



**HAL**  
open science

# Influence of pH on the interlayer cationic composition and hydration state of Ca-montmorillonite: analytical chemistry, chemical modelling and XRD profile modelling study.

Eric Ferrage, Christophe Tournassat, Emmanuel Rinnert, Bruno Lanson

## ► To cite this version:

Eric Ferrage, Christophe Tournassat, Emmanuel Rinnert, Bruno Lanson. Influence of pH on the interlayer cationic composition and hydration state of Ca-montmorillonite: analytical chemistry, chemical modelling and XRD profile modelling study.. *Geochimica et Cosmochimica Acta*, 2005, 69, pp.2797-2812. 10.1016/j.gca.2004.12.008 . hal-00106998

**HAL Id: hal-00106998**

**<https://hal.science/hal-00106998>**

Submitted on 17 Oct 2006

**HAL** is a multi-disciplinary open access archive for the deposit and dissemination of scientific research documents, whether they are published or not. The documents may come from teaching and research institutions in France or abroad, or from public or private research centers.

L'archive ouverte pluridisciplinaire **HAL**, est destinée au dépôt et à la diffusion de documents scientifiques de niveau recherche, publiés ou non, émanant des établissements d'enseignement et de recherche français ou étrangers, des laboratoires publics ou privés.

# **Influence of pH on the interlayer cationic composition and hydration state of Ca-montmorillonite: analytical chemistry, chemical modelling and XRD profile modelling study**

**Revised Version n°2**

ERIC FERRAGE,<sup>1,2,\*</sup> CHRISTOPHE TOURNASSAT,<sup>2,3</sup> EMMANUEL RINNERT<sup>2,4</sup>  
and BRUNO LANSON<sup>1</sup>

<sup>1</sup> Environmental Geochemistry Group, LGIT, University of Grenoble-I P.O. Box 53, 38041 Grenoble, France.

<sup>2</sup> ANDRA, Parc de la Croix Blanche, 1/7 rue Jean Monnet, 92298 Châtenay-Malabry Cedex, France

<sup>3</sup> BRGM, 3 avenue Claude Guillemin, 45060 Orléans Cedex 2, France

<sup>4</sup> Laboratoire de Chimie Physique et Microbiologie pour l'Environnement, UMR 7564 CNRS- Université Henri Poincaré, 405 rue de Vandoeuvre, 54600 Villers-Lès-Nancy, France

\* Corresponding author:

Eric Ferrage

Fax: +33 (0)4 7682 8101;

Tel: +33 (0)4 7682 8018;

E-mail: [eric.ferrage@obs.ujf-grenoble.fr](mailto:eric.ferrage@obs.ujf-grenoble.fr);

Keywords : smectite, hydration state, XRD modelling, pH, chemical modelling, interlayer protons

## ABSTRACT

The hydration state of a <2  $\mu\text{m}$  fraction of Ca-saturated SWy-2 montmorillonite was characterised after rapid equilibration (3 hours) under pH-controlled conditions (0.1-12.6 pH range). The solution composition was monitored together with the interlayer composition and X-ray diffraction (XRD) patterns were recorded on oriented preparations. Experimental XRD patterns were then fitted using a trial-and-error procedure to quantify the relative proportions of layers with different hydration states.

The montmorillonite is mostly bi-hydrated in basic and near-neutral conditions whereas it is mostly mono-hydrated at low pH. The transition from the bi-hydrated to the mono-hydrated state occurs through very heterogeneous structures. However, the proportion of the different layer types determined from XRD profile modelling and that derived from chemical modelling using Phreeqc2 code strictly coincide. This correlation shows that the hydration modification is induced by a  $\text{H}_3\text{O}^+$ -for- $\text{Ca}^{2+}$  exchange at low pH, the two species being distributed in different interlayers. This layer-by-layer exchange process occurs randomly in the layer stack.

Under alkaline conditions, results from XRD profile modelling and from near infrared diffuse reflectance spectroscopy (NIR-DRS) clearly demonstrate that there is no  $\text{CaOH}^+$ -for- $\text{Ca}^{2+}$  exchange at high pH. The apparent increase in Ca sorption in smectite interlayers with increasing pH is thus probably related to the precipitation of Calcium-Silicate-Hydrate (CSH) phases, which also accounts for the decrease in Si concentration under high-pH conditions. This precipitation is thermodynamically favoured.

## 1. INTRODUCTION

One of the possible multi-barrier storage concepts developed in France for intermediate-level long-lived radioactive wastes (ILLW wastes) consists of vitrified waste placed in containers and overpacks, encased in exogenous materials (near-field engineered barrier) and ultimately buried in a clay-rich geological formation (far-field barrier). Bentonite, a clay material mostly constituted of smectite, is considered a promising material as an engineered barrier in the context of nuclear waste disposal. The potential of smectite stems from its mechanical self-healing ability, its low hydraulic conductivity and its high sorption capacities, the combination of which is assumed to help prevent or delay radionuclide migration. However, the initial properties of smectite could be altered significantly by storage-induced perturbations. For example, the use of concrete for waste overpacks or the oxidation of pyrite, which is often present as an accessory mineral in the relevant geological environments, can lead to a wide pH range for solutions saturating the clay-barriers.

Substitutions in either tetrahedral or octahedral sheets of the smectite structure induce a permanent negative layer charge that is balanced by the presence of hydrated cations in the interlayer space. The interlayer cation composition of smectite has been studied for many decades as a function of the composition of the solution in contact with clay surfaces (Vanselow, 1932a; Sposito, 1981 and references therein), and the thermodynamics of cation exchange have been developed specifically to model these interlayer cation compositions (Vanselow, 1932a; Sposito, 1977, 1981, 1984; Elprince et al., 1980; Shainberg et al., 1980; Shu-Yuan and Sposito, 1981; Sposito et al., 1981, 1983a, 1983b, 1999; Fletcher and Sposito, 1989; Delville, 1991; Appelo and Postma, 2000). Smectite cation exchange affinities have been established for a wide range of cations including protons, which possibly replace interlayer cations under acidic conditions (Fletcher and Sposito, 1989 and reference therein).

26 For the most common interlayer cations, hydration of homoionic smectites has been  
27 extensively studied and it has been shown, most often from the variation of 00 $l$  basal  
28 reflection d-spacings, that smectite incorporates H<sub>2</sub>O molecules in its interlayers. As a  
29 consequence, with increasing relative humidity the smectite structure “swells” in different  
30 steps corresponding to the intercalation of 0, 1, 2 or 3 layers of H<sub>2</sub>O molecules  
31 (Nagelschmidt, 1936; Bradley et al., 1937; Mooney et al., 1952; Norrish, 1954; Walker,  
32 1956). From these early studies, it is now accepted that the hydration ability of 2:1  
33 phyllosilicates is controlled by factors such as the nature of the interlayer cation and the  
34 amount of layer charge and its location (octahedral vs. tetrahedral). These observations have  
35 led to different models in which crystalline swelling is controlled by the balance between the  
36 repulsive forces between adjacent 2:1 layers and the attractive forces between hydrated  
37 interlayer cations and the negatively charged surface of 2:1 layers (Norrish, 1954; Van  
38 Olphen, 1965; Kittrick, 1969a, 1969b; Laird, 1996, 1999). The few studies devoted to the  
39 hydration of bi-ionic smectites (Glaeser and Méring, 1954; Levy and Francis, 1975), and  
40 (Iwasaki and Watanabe, 1988) on (Na, Ca)-smectites and (Mamy and Gaultier, 1979) on (K,  
41 Ca)-smectites) have shown that interlayer cations tend to distribute in distinct interlayers  
42 leading to a “demixed” state.

43 The present work aims at characterising the hydration state of an initially Ca-  
44 saturated montmorillonite as a function of pH in order to better predict smectite reactivity  
45 under disturbed chemical conditions, such as those likely to occur in the vicinity of a nuclear  
46 waste disposal. For this purpose, the combination of chemical modelling and XRD profile  
47 modelling were used to follow the exchange of Ca<sup>2+</sup> cations by protons under acidic  
48 conditions. Specific X-ray diffraction modelling techniques based on a trial-and-error  
49 approach were used to refine the early descriptions of smectite hydration by taking into  
50 account the possible coexistence in the smectite structure of different layer types, each

51 exhibiting a specific hydration state (Bérend et al., 1995; Cases et al., 1997; Cuadros, 1997;  
52 Ferrage et al., 2005a, 2005b). In particular, the likely mutual exclusion of calcium and protons  
53 in smectite interlayers and the expected hydration contrast between such calcium- and proton-  
54 saturated smectite layers was used to follow the  $\text{H}_3\text{O}^+$ -for- $\text{Ca}^{2+}$  exchange supposed to occur at  
55 low pH. The same techniques were also used to assess the possible presence of cation –  
56 hydroxide ions pairs under alkaline conditions proposed by Tournassat et al. (2004a, 2004b)  
57 and Charlet and Tournassat (2005) on the basis of cation exchange experiments and chemical  
58 modelling.

59

60 ----- The following section to be typed in smaller characters -----

61

## 62 **2. MATERIALS AND METHODS**

63

### 64 **2.1 Clay material preparation**

65

66 The smectite used for this study was the SWy-2 montmorillonite reference from the  
67 Source Clays Repository of The Clay Minerals Society  
68 (<http://www.agry.purdue.edu/cjohnston/sourceclays/index.html>) with structural formula  
69 (Stucki et al., 1984):  $[(\text{Al}_{3.01} \text{Fe}_{0.43} \text{Mg}_{0.56})(\text{Si}_{7.97} \text{Al}_{0.03})\text{O}_{20}(\text{OH})_4] \text{M}^{+0.72}$ . Naturally, this  
70 montmorillonite is mostly Na-saturated, and exhibits a low octahedral charge deficit and  
71 extremely limited tetrahedral substitutions (Mermut and Lagaly, 2001).

72 Size fractionation was performed by centrifugation to obtain a suspension of the  
73  $<2 \mu\text{m}$  size fraction. An ion-exchange process was then carried out on this clay separate at  
74 room temperature with  $1 \text{ mol.L}^{-1}$  aqueous saline solution of  $\text{CaCl}_2$ . The SWy-2 suspension  
75 was shaken mechanically in this saline solution for 24h before separation of the solid fraction

76 by centrifugation and addition of fresh saline solution. This step was repeated three times to  
77 ensure complete cation exchange. Excess salts were then washed by four 24h cycles,  
78 including sedimentation, removal of the supernatant and re-suspension in deionised water  
79 (milli-Q/18.2 M $\Omega$  cm<sup>-1</sup>). The clay content of the final Ca-SWy-2 suspension was found to be  
80 ~37g of clay per kg of suspension using the weighing method given by Sposito et al. (1981)  
81 and revised by Tournassat et al. (2004a).

82

## 83 **2.2 Sample preparation**

84

85 Centrifugation tubes were precisely weighed ( $m_{tube}$  in g) with a Mettler Toledo  
86 AG285 balance. A ~3mL aliquot of the Ca-SWy-2 suspension was introduced into each  
87 50 mL centrifuge tube with a calibrated micropipette ( $V_{susp}$ , clay content  $\rho$ ). Variable volumes  
88 of Ca(OH)<sub>2</sub> or HCl were then added to reach the desired pH after addition of deionised water  
89 to obtain a 40 mL total volume ( $V_{tot}$ ). The tubes were shaken for three hours. A 15mL  
90 suspension aliquot was then collected from each tube, precisely weighed ( $V_{XRD}$ ) and used for  
91 X-ray diffraction (XRD) data collection (see below). The remaining suspension was  
92 centrifuged to separate the solution from the clay slurry.

93 An aliquot of supernatant fluid from each tube was further filtered (0.20  $\mu$ m) before  
94 measuring the pH with a pH-microelectrode (Mettler Toledo, InLab 423). Another aliquot  
95 was filtered for Na, Ca, Si, Al, Mg and Fe concentration measurements ( $C_{sol}^{elt}$ , where  $elt$   
96 represents Ca, Si, etc.) using a Perkin-Elmer Optima 3300 DV inductively coupled plasma  
97 atomic emission spectrometer (ICP-AES). Si, Al, Mg and Fe concentrations were measured  
98 on a third supernatant aliquot obtained without prior filtration to give the mass of suspended  
99 solids in the supernatant as explained in Tournassat et al. (2004a) ( $m_{correction}$ ). On the other  
100 hand, the centrifuge tubes containing the clay slurry were weighed precisely ( $m_{centrif}$ ) and 30

101 mL ( $V_{Amm}$ ) of 1 M ammonium acetate were added to each tube, each tube being precisely  
 102 weighed after ammonium acetate addition ( $m_{Amm}$ ) and shaken for 24h.  $NH_4^+$  cations are meant  
 103 to replace  $Ca^{2+}$  cations in the smectite interlayer (e.g. Sposito et al., 1981, 1983a, 1983b) and  
 104 the subsequent measurement of  $Ca^{2+}$  concentration in the supernatant solution leads to the  
 105 Calcium Cation Exchange Capacity (Ca-CEC). Since some solution remained in the clay  
 106 slurry ( $V_{slurry}$ ) before the addition of ammonium acetate, the volume of supernatant was equal  
 107 to the volume of added ammonium acetate plus this volume of solution in the slurry  
 108 ( $V_{Amm+slurry}$ ). Furthermore, the amount of  $Ca^{2+}$  present in the remaining slurry solution ( $C_{sol}^{Ca}$   
 109  $\times V_{slurry}$ ) must be subtracted from the amount of Ca in the supernatant ( $C_{Amm}^{Ca} \times V_{Amm+slurry}$ ).  
 110 Hence, Ca-CEC is given by the following formula (in eq.kg<sup>-1</sup>, i.e. in mol of charge per kg of  
 111 clay):

$$112 \quad Ca - CEC = 2 \times \frac{C_{Amm}^{Ca} \times V_{Amm+slurry} - C_{sol}^{Ca} \times \left( m_{centrif} - m_{tube} - \left( V_{susp} \times \frac{V_{tot} - V_{XRD}}{V_{tot}} \times \rho \right) \right)}{\left( V_{susp} \times \frac{V_{tot} - V_{XRD}}{V_{tot}} \times \rho \right) - m_{correction}}, \quad (1)$$

$$113 \quad \text{with } V_{Amm+slurry} = \frac{m_{Amm} - m_{tube} - \left( V_{susp} \times \frac{V_{tot} - V_{XRD}}{V_{tot}} \times \rho \right)}{d_{Amm}} \quad (2)$$

114 where volumes (V) are in L, concentrations (C) in mol.L<sup>-1</sup>, clay content ( $\rho$ ) in g.L<sup>-1</sup> and  
 115 masses (m) in g. The density of all solutions was assumed to be equal to 1.0, except for the  
 116 density of the 1 M ammonium solution ( $d_{Amm} = 1.077$ ).

117

### 118 **2.3 Chemical composition modelling**

119

120 The chemical modelling used in this study was performed using the Phreeqc2 code  
 121 (Parkhurst and Appelo, 1999), since this versatile computer code is amenable to the various



122 conventions used to describe cation exchange and surface complexation. The model used for  
123 cation exchange was similar to that developed by Tournassat et al. (2004a) and only the main  
124 concepts and parameters are described to simplify understanding. Cation exchange capacity of  
125 montmorillonite originates both from the presence of a permanent negative charge ( $\sigma_0$ ) in the  
126 clay lattice resulting from octahedral and tetrahedral substitutions and from the presence of  
127 broken bonds at the edges of clay platelets, which induces a pH-dependent charge ( $\sigma_H$ ). By  
128 combining a cation-exchange model based on the Vanselow convention (Vanselow, 1932a;  
129 Sposito, 1981) with the pH-dependent charge model developed by Tournassat et al. (2004b)  
130 for clay minerals, the evolution of the Ca-CEC value can be modelled as a function of pH.  
131 Key parameters are cation exchange selectivity coefficients ( $K_{int}$  - Table 1), clay permanent  
132 charge ( $\sigma_0$ ), structural formula and edge surface area. The latter parameter was considered to  
133 be equal to that determined for the fine fraction of the commercial Wyoming bentonite MX80  
134 montmorillonite ( $8.5 \text{ m}^2.\text{g}^{-1}$ , Tournassat et al., 2003). From the adjustment to Ca-CEC data,  
135 the  $\sigma_0$  value was taken to be  $0.94 \text{ mol of charge (mol}_c\text{) per kg of clay}$ . This value is similar,  
136 within error, to the  $1.0 \text{ mol}_c.\text{kg}^{-1}$  value calculated from the structural formula. In the model  
137 used, a decrease of Ca-CEC was interpreted either as a decrease of  $\sigma_H$  (typically from pH 4 to  
138 10 in the present study) or as resulting from  $\text{H}^+$  sorption in the interlayer.

139

#### 140 **2.4 X-ray diffraction analysis and profile modelling**

141

142 For XRD analysis, suspension aliquots were poured through a Millipore filter  
143 ( $0.4\mu\text{m}$ ) and the clay cake was then laid down on a previously weighed glass slide. The  
144 resulting oriented preparations were then dried at room temperature and the mass of smectite  
145 on the glass slide was precisely determined. XRD patterns were then recorded using a Bruker  
146 D5000 diffractometer equipped with an Ansyco rh-plus 2250 humidity control device coupled

147 to an Anton Paar TTK450 chamber. Data collection was performed at 40% relative humidity  
148 (RH) after an homogenisation period of 15 min before the measurement. Experimental  
149 measurement parameters were 6s counting time per  $0.04^\circ 2\theta$  step. The divergence slit, the two  
150 Soller slits, the antiscatter slit and the resolution slit were  $0.5^\circ$ ,  $2.3^\circ$ ,  $2.3^\circ$ ,  $0.5^\circ$  and  $0.06^\circ$ ,  
151 respectively. For each sample, XRD patterns were collected over a time span not exceeding  
152 one day after glass slide preparation.

153         The algorithms developed initially by Sakharov and Drits (1973), Drits and Sakharov  
154 (1976) and more recently by Drits et al. (1997a) and Sakharov et al. (1999) were used to fit  
155 experimental XRD profiles over the  $2\text{--}50^\circ 2\theta$   $\text{CuK}\alpha$  range using a trial-and-error approach.  
156 Instrumental and experimental factors such as horizontal and vertical beam divergences,  
157 goniometer radius, length and thickness of the oriented slides were measured and introduced  
158 without further adjustment. The mass absorption coefficient ( $\mu^*$ ) was set to  $45 \text{ cm}^2 \cdot \text{g}^{-1}$ , as  
159 recommended by Moore and Reynolds (1997) for clay minerals, whereas the parameter  
160 characterising the preferred orientation of the sample ( $\sigma^*$ ) was considered as a variable  
161 parameter. The z-coordinates for all atoms within the 2:1 layer framework were set as  
162 proposed by Moore and Reynolds (1997). The z-coordinates of interlayer species for  
163 dehydrated (0W) and mono-hydrated (1W) smectite layers were also set as proposed by  
164 Moore and Reynolds (1997), in contrast to those for bi-hydrated (2W) layers, since a more  
165 realistic description of the interlayer structure is obtained by assuming a unique plane of  $\text{H}_2\text{O}$   
166 molecules on either side of the central interlayer cation (Ferrage et al., 2005a). The distance  
167 along the  $c^*$  axis from the interlayer cation plane and the  $\text{H}_2\text{O}$  molecule plane is  $\sim 1.2 \text{ \AA}$ .

168         Additional variable parameters include the coherent scattering domain size (CSDS)  
169 along the  $c^*$ -axis, which was characterised by a maximum CSDS, set at 45 layers, and a mean  
170 CSDS value ( $N$  – Drits et al., 1997b), which was adjusted. In addition, because of the weak  
171 bonding between adjacent smectite layers, layer thickness is probably scattered about its

172 average value. This cumulative deviation from strict periodicity, described by Guinier (1964)  
173 as a disorder of the second type and detailed later by Drits and Tchoubar (1990), can be  
174 considered as strains and was accounted for by introducing a deviation parameter ( $\sigma_z$ ). The  
175 overall fit quality was assessed using the  $R_p$  parameter (Howard and Preston, 1989). This un-  
176 weighted parameter was preferred because it is mainly influenced by misfits on the most  
177 intense diffraction maxima such as the 001 reflection, which contains essential information on  
178 the proportions of the different layer types and on their respective layer thickness

179         The fitting procedure described in detail by Ferrage et al. (2005a) was used for all  
180 experimental XRD profiles of exchanged Ca-SWy. Briefly, a main structure, periodic when  
181 possible, was used to reproduce as much as possible of the experimental XRD pattern. If  
182 necessary, additional contributions to the diffracted intensity were introduced to account for  
183 the lack of fit between calculated and experimental patterns. These extra contributions were  
184 systematically related to mixed-layered structures (MLS) containing two or three components,  
185 randomly interstratified. Up to four structures were necessary to reproduce experimental  
186 patterns, because of the very heterogeneous structures observed. However, layers with the  
187 same hydration state present in the different MLS contributing to the diffracted intensity were  
188 assumed to have identical properties to reduce the number of adjustable parameters.  
189 Specifically for a given sample, each given layer type (0W, 1W or 2W layers) was provided  
190 with a unique chemical composition, a unique layer thickness, and a unique set of atomic  
191 coordinates for all contributions. Similarly, identical values of the  $\sigma^*$ , N and  $\sigma_z$  parameters  
192 were used at a given pH value for all MLSs, even though these parameters were nevertheless  
193 allowed to vary as a function of pH. The relative proportions of the different MLSs and that of  
194 the different layer types in these MLSs were also considered as variable parameters during the  
195 fitting procedure.

196 The fitting strategy is illustrated in Figure 1 for the XRD pattern obtained for Ca-  
197 Swy-2 equilibrated in deionised water (pH = 6.41). Qualitatively, the experimental pattern  
198 exhibits well-defined diffraction maxima forming a rational series with a  $d_{001}$  value  
199 characteristic of a bi-hydrated state ( $\sim 15.20$  Å). However, a significant asymmetry is visible  
200 on the high-angle side of the 001 and 003 reflections and on both sides of the 005 reflection  
201 (arrows in Figure 1a) as demonstrated by the difference plot between the experimental pattern  
202 and that calculated for the contribution of pure bi-hydrated smectite (100% of 2W layers).  
203 According to the Méring principle (Méring, 1949), the residual maximum on the high-angle  
204 side of the 001 reflection can be attributed to a MLS containing layers with a lower layer  
205 thickness in addition to 2W layers. Accordingly, a satisfactory fit ( $R_p = 1.45\%$ ) was obtained  
206 when a second contribution ( $S2 - S1:S2 = 87:13$ ), resulting from the random  
207 interstratification of 2W, 1W and 0W layers (60%, 30% and 10%, respectively – Figs. 1b, c),  
208 was added to the initial contribution (S1), as schematised by the pictogram shown in Figure  
209 1d. In this pictogram, the relative proportions of the two MLSs contributing to the diffracted  
210 intensity are represented along the vertical axis by their respective surface areas whereas the  
211 proportions of the different layer types in each structure are represented on the horizontal axis.  
212 Overall, this sample contains 95% of 2W layers, 4% of 1W layers and 1% of 0W layers.

213 One may note that the calculated XRD patterns are not plotted over the low angle  
214 region ( $2\theta$  angles lower than  $5^\circ$ ) because the shape of the computed “background” over this  
215 angular range is not consistent with that of experimental patterns. The origin of this  
216 discrepancy is discussed by Ferrage et al. (2005a) using the recent theoretical developments  
217 made by Plançon (2002). These new insights into the real structure of clay aggregates may  
218 make it possible to reproduce experimental patterns over this angular range but they would  
219 not bring into question the results reported in the present manuscript.

220

## 221 2.5. Near Infrared Diffuse Reflectance analysis

222

223 Near infrared diffuse reflectance (NIR-DR) spectra were recorded using a Perkin-  
224 Elmer 2000 FTIR spectrometer equipped with a deuterated triglycine sulphate (DTGS)  
225 detector, a tungsten-halogen source and a quartz beam-splitter. The optical device used is  
226 based on the Harrick© equipment. Diffuse reflectance spectra were recorded from 4000 to  
227 8000  $\text{cm}^{-1}$  with a spectral resolution of 8  $\text{cm}^{-1}$  and obtained from the addition of 50 individual  
228 scans. Samples were placed into a Harrick© cell in which the temperature and pressure were  
229 controlled from 25-100°C and from  $10^{-4}$ - $10^5$  Pa, respectively. Sample temperature was  
230 measured to an accuracy greater than 0.1°C using a Pt resistance. The spectra of hydrated  
231 samples equilibrated at room humidity ( $40 \pm 5\%$ ) were recorded first. The samples were  
232 subsequently out-gassed at 60°C for 16 hours under a residual pressure of  $5 \cdot 10^{-3}$  Pa by using a  
233 two-stage pump comprising a scroll pump and a turbomolecular pump. Two complementary  
234 gauges (Pirani and ionisation types) were used to measure the pressure from  $10^{-4}$  Pa to room  
235 pressure. Spectra were then recorded at a sample temperature of 25°C under a residual  
236 pressure of  $5 \cdot 10^{-4}$  Pa. The diffuse reflectance,  $R$ , is defined as:

$$237 \quad R = -\log \frac{I_s^D(\sigma)}{I_0^D(\sigma)} \quad (3)$$

238 where  $I_s^D$  is the collected diffused irradiance of the sample,  $I_0^D$  the collected diffused  
239 irradiance of the reference and  $\sigma$  the wavenumber. The reference was taken at 24.8°C from a  
240 potassium bromide ground powder subsequently dried under a residual pressure of  $5 \cdot 10^{-3}$  Pa.

241 For clay samples, the spectral domain presented in this study can be split into two  
242 regions. From 4550 to 5500  $\text{cm}^{-1}$ , only  $\text{H}_2\text{O}$  molecules can be observed from the combinations  
243 of stretching and bending modes. From 6500 to 7500  $\text{cm}^{-1}$ , overtones of stretching modes of  
244 all hydroxyl groups, both from interlayer  $\text{H}_2\text{O}$  molecules and from the silicate framework, are

245 visible (Burneau et al., 1990; Madejova et al., 2000b). As fundamental stretching modes of  
246 hydroxyl groups have been reported previously over the 3370-3670  $\text{cm}^{-1}$  range (Madejova et  
247 al., 2000a; Vantelon et al., 2001; Bishop et al., 2002), the frequency range calculated for the  
248 first stretching overtone extends from 6575-7175  $\text{cm}^{-1}$ , assuming a 82.5  $\text{cm}^{-1}$  anharmonicity  
249 coefficient for OH groups (Burneau and Carteret, 2000).

250

251 ----- End of the section to be typed in smaller characters -----

252

253

### 3. RESULTS

254

#### 3.1. Cation concentrations in solution and in the clay interlayer

255

256  
257 Concentrations of Ca, Al, Fe and Mg cations in solution are plotted as a function of  
258 pH in Figure 2. As observed in earlier studies (Baeyens and Bradbury, 1997; Tournassat et al.,  
259 2004a), the concentrations of Al, Fe and Mg in solution increase under low pH conditions as a  
260 result of clay dissolution and/or desorption processes. In addition, below a pH value of about  
261 3, Ca concentration in solution dramatically increases as the pH decreases, although no Ca is  
262 added. At the same time, the apparent amount of Ca sorbed in the clay interlayer decreases  
263 (Fig. 3), whereas no other cation, such as Na, Al, Fe or Mg, appears to be sorbed in the  
264 interlayer from  $\text{NH}_4^+$  exchange experiment results. With decreasing pH,  $\text{Ca}^{2+}$  is thus certainly  
265 replaced by protons in the smectite interlayer as previously hypothesized (Gilbert and  
266 Laudelout, 1965; Fletcher and Sposito, 1989; Bradbury and Baeyens, 1997; Tournassat et al.,  
267 2004b).

268 Under high pH conditions ( $\text{pH} > 12$ ), the addition of  $\text{Ca}(\text{OH})_2$  to the clay suspension  
269 leads both to an increase in the Ca concentration in solution and to an increase in the apparent

270  $\text{Ca}^{2+}$  sorption on smectite (Figs. 2a, 3). From these observations, and specifically from the  
271 concomitant increase in  $\text{OH}^-$  sorption, Tournassat et al. (2004a, 2004b) have hypothesized the  
272 sorption of  $\text{CaOH}^+$  ion pairs in the smectite interlayers, as observed for  $\text{CaCl}^+$  when ionic  
273 strength is high (Sposito et al., 1983a, 1983b; Tournassat et al., 2004b; Ferrage et al., 2005c).  
274 However, the concentration of Si in solution decreases simulatenously with the apparent  
275 increase of  $\text{Ca}^{2+}$  sorption on smectite (Fig. 3). This correlation possibly indicates the  
276 precipitation of a tobermorite-like Ca-Si phase at high pH (Claret et al., 2002; Tournassat et  
277 al., 2004a, 2004b) as discussed below. This hypothesis is also supported by the steady  
278 evolution of solution chemistry reported by Tournassat et al. (2004a) when working in a  $\text{Na}^+$   
279 ionic medium rather than in a  $\text{Ca}^{2+}$  one. However, sorption of  $\text{CaOH}^+$  ion pairs cannot be  
280 differentiated from the precipitation of a Ca-Si phase on the sole basis of analytical chemistry  
281 experiments. As a consequence, modelling of XRD experiments was carried out in order to  
282 characterise the clay structural changes associated with the observed chemical evolutions, and  
283 to assess the various hypotheses arising from chemical modelling.

284

### 285 **3.2. Solid characterisation under acidic conditions**

286 The qualitative observation of the 001 reflection recorded at a constant RH value  
287 (40%) for samples equilibrated at different pH values shows a dramatic modification of the  
288 smectite hydration state with decreasing pH (Fig. 4a), most probably resulting from the  
289 modification of the smectite interlayer composition. Near neutral pH, smectite is mainly bi-  
290 hydrated ( $d_{001} \sim 15.2 \text{ \AA}$ ), whereas at low pH values (e.g. 0.14) the presence of protons in the  
291 smectite interlayer leads to the shift of the 001 reflection towards lower  $d_{001}$  ( $\sim 12.6 \text{ \AA}$ ), which  
292 are characteristic of 1W smectites. When decreasing the pH from near neutral condition (pH =  
293 6.41), the steady decrease of the 001 reflection intensity and the increase of the asymmetry on  
294 its high-angle side are consistent with the continuous incorporation of 1W layers. Extremely

295 heterogeneous structures, most probably corresponding to the interstratification of 2W and  
296 1W layers, are observed at intermediate pH values (e.g. 1.41), whereas at lower pH values, the  
297 steady increase in the 12.6 Å peak intensity and its sharpening are indicative of a  
298 homogeneous 1W state.

299 In the modelling of these experimental XRD patterns, it was assumed that the 1W  
300 and 2W layers correspond to smectite layers saturated with protons and  $\text{Ca}^{2+}$  cations,  
301 respectively. This hypothesis is strongly supported by the overwhelming presence of 2W  
302 layers in low-charge montmorillonite equilibrated at 40% RH (Ferrage et al., 2005a). In  
303 addition, for layers saturated by protons, it was assumed that the layer charge compensation  
304 was achieved by  $\text{H}_3\text{O}^+$  cations, as the difference between  $\text{H}_3\text{O}^+$  or  $\text{H}^+$  cations could not be  
305 differentiated from the presence of an additional  $\text{H}_2\text{O}$  molecule on the mid-plane of the  $\text{H}^+$ -  
306 saturated interlayer. Finally, because X-ray diffraction is only sensitive to the electronic  
307 density, a simple calculation of the scattering factor for  $\theta = 0$  weighted to the cation valency  
308 ( $\eta$  index) shows that it is not possible to differentiate, from the diffracted intensity, between  
309 interlayers saturated by  $\text{Ca}^{2+}$  or  $\text{H}_3\text{O}^+$  cations.  $\text{Ca}^{2+}$  cations contain  $18e^-$  and therefore  $\eta = 9e^-$   
310 per charge unit (c.u.) whereas for  $\text{H}_3\text{O}^+$  ions  $\eta = 10 e^-/\text{c.u.}$  This calculation shows that the  
311 systematic presence of protons as interlayer cations in 1W, which was initially assumed, will  
312 not significantly impact the proportion of the different layer types derived from XRD profile  
313 modelling.

314 The calculated profiles are compared to the experimental patterns in Figure 5 and the  
315 relative contributions to the diffracted intensity as a function of pH are schematised in Figure  
316 6 together with the composition of the associated MLSs. The relative contributions of the  
317 different MLSs to the diffracted intensity and their evolution as a function of pH are  
318 illustrated in Figure 7 for characteristic XRD patterns. Additional structural parameters, such



319 as the layer thickness of the different layer types, their content of H<sub>2</sub>O molecules, the number  
320 N of layers building up CSDs,  $\sigma^*$  and  $\sigma_z$  are listed in Table 2.

321 A similar model was found for pH values of 6.41 and 5.98. This model, which is  
322 described in the method section, includes both a periodic structure containing only 2W layers  
323 and a MLS containing the three layers types (2W:1W:0W ratio 60:30:10 – Figs. 1, 5, 6). The  
324 relative abundance of the MLS increases slightly at the expense of the periodic one as pH  
325 decreases (Fig. 6). Structure models obtained for the pH values down to 2.88 are quite similar  
326 to the previous one, differing only in the presence of a small amount (~2%) of 1W layers in  
327 the former periodic structure (Fig. 6). Again, the relative contribution of the most  
328 homogeneous structure decreases with decreasing pH. For pH values between 2.46 and 1.93,  
329 all attempts to reproduce experimental XRD patterns with two contributions were  
330 unsuccessful. As the asymmetry on the high angle side of the 001 reflection becomes more  
331 pronounced (Figs. 5, 7) it was necessary to introduce a third contribution. As compared to the  
332 previous two contributions, this additional MLS must incorporate a noticeable amount of 1W  
333 layers to account for the observed asymmetry. The optimum composition determined for this  
334 additional MLS was a 2W:1W:0W ratio of 30:60:10 (Figs. 5, 6). In addition, the composition  
335 of the mostly bi-hydrated structure was modified to increase the content of 1W layers up to  
336 5% for these pH values between 2.46 and 1.93. The contributions of the different MLS to the  
337 XRD pattern recorded for sample pH = 1.93 are illustrated in Figure 7a, in which it is possible  
338 to observe the contribution of the additional MLS as a broad modulation at ~14°2 $\theta$ .

339 When lowering the pH value to 1.75, it was again necessary to consider an additional  
340 contribution to the diffracted intensity in order to satisfactorily fit the experimental XRD  
341 pattern (Figs. 5, 6, 7b). In Figure 7b, the maximum at ~14°2 $\theta$  now appears as a better-defined  
342 peak as compared to Figure 7a, the position of this well-defined maximum indicating that this  
343 additional MLS is essentially mono-hydrated. The additional presence of this new MLS

344 (1W:0W ratio 99:1) allows a satisfactory fit to the experimental XRD profile. In Figure 7b,  
345 one may also note the presence on the high-angle side of the 001 reflection of broad  
346 modulations whose positions are consistent with those of the various MLSs contributing to  
347 the calculated intensity. The very heterogeneous structure observed at pH 1.41 (Figs. 6, 7c)  
348 was modelled using the same four MLSs as those reported for the previous sample. The  
349 composition of these four structures was kept constant for the two samples (pH 1.75 and  
350 1.41), the fit of the experimental profile being achieved by varying the relative proportions of  
351 the various MLSs (Figs. 5, 6, 7c). A similar model was used to fit the experimental XRD  
352 pattern recorded at pH 1.28 (Figs. 5, 6, 7d). In this model, variation of the relative proportion  
353 of the different MLSs accounts for most of the profile modification in addition to a limited  
354 decrease of the 2W layer content in one of the MLSs. As for the sample at pH = 1.75,  
355 modulations, now observed on the low-angle side of the 001 reflection, allow the composition  
356 of the different contributions (Fig. 7d) to be defined. On XRD patterns recorded at pH values  
357 of 0.98 and 0.14, the 001 reflection appears sharper and more symmetrical, thus allowing a  
358 satisfactory fit with only two contributing MLSs (Figs. 5, 6, 7e). The first MLS accounts for  
359 most of the diffracted intensity and corresponds to an almost periodic 1W structure, whereas a  
360 second MLS (2W:1W:0W ratio 30:40:30) enables the “tails” of the 001 reflection to be fitted  
361 (Figs. 6, 7e). With decreasing pH, the content of 2W layers slightly decreases in the latter  
362 MLS (Fig. 6).

363 While fitting all the XRD patterns collected under acidic conditions, special attention  
364 was paid to keep layer thickness constant for all three layer types (2W, 1W, and 0W – Table  
365 2). In addition, for a given sample, the layer and crystal parameters were kept identical for all  
366 the MLS, and only the composition and the relative proportions of the different MLSs was  
367 allowed to vary. Most structural parameters were found constant with pH, except for the size  
368 of CSDs and  $\sigma_z$ , which decrease with decreasing pH, whereas the water content slightly

369 increases in 1W layers (Table 2). The relative proportions of the different layer types are  
370 plotted in Figure 8 as a function of pH to highlight the change in hydration state induced by  
371 the progressive exchange of  $\text{H}_3\text{O}^+$  for interlayer cations as pH decreases.

372

### 373 **3.3. Solid characterisation under basic conditions**

374

375 No significant change in the 001 reflection profile is observed over the basic pH  
376 range (Fig. 4b), except for a limited shift of the position from 15.20 Å for near neutral pH  
377 conditions to 15.15 Å at pH = 12.62. The extremely similar XRD profiles observed over the  
378 whole angular domain (Figs. 4b, 9) are indicative of a constant hydration state over the whole  
379 basic pH range. This is confirmed by the comparison between the experimental and calculated  
380 XRD patterns (Fig. 9) and by the structure models reported in Figure 10 and further detailed  
381 in Table 3. A model similar to that obtained in near neutral conditions (Fig. 1) was used to  
382 reproduce the experimental patterns. This model consists of two structures, the first one  
383 containing exclusively (6.41-9.59 pH range) or mostly (11.24-12.62 pH range) 2W layers,  
384 whereas the three layer types are present in the second MLS (Fig. 10). The relative  
385 proportions of the two structures (Fig. 10) and that of the different layer types (Fig. 8) are  
386 about constant over the basic pH range. Most structural parameters were also found to be  
387 constant over the basic pH range since only a limited increase in the number of layers in the  
388 CSDs and a slight decrease of the layer thickness for 2W layers were observed with  
389 increasing pH (Table 3).

390

391

## 4. DISCUSSION

### 4.1. $\text{H}_3\text{O}^+$ -for- $\text{Ca}^{2+}$ exchange at low pH

#### 4.1.1. $\text{H}_3\text{O}^+$ -for- $\text{Ca}^{2+}$ exchange. XRD vs. chemical modelling

Under acidic conditions, a dramatic change in the hydration state is observed as pH decreases from the position of the 001 reflection, which shifts from 15.2 Å (2W layers) under near-neutral conditions to 12.6 Å (1W layers) under low pH conditions. As Ca-saturated low-charge montmorillonite is predominantly bi-hydrated at 40% RH, this modification may be linked to the progressive exchange of protons for interlayer  $\text{Ca}^{2+}$  that can be deduced from the chemical data (Fig. 3). This data can be simulated with the model given by Tournassat et al. (2004a, 2004b) to deduce the interlayer chemical composition as a function of pH (Fig. 11). The cation exchange reaction selectivity coefficients ( $K_{int}$ ) reported by Tournassat et al. (2004a) were used (Table 1), whereas the structural CEC was adjusted to a consistent 0.94 eq.kg<sup>-1</sup> value; no other parameter was fitted. Interlayer composition modelling confirms that Na, Al, Fe or Mg do not sorb in the interlayer to a significant extent (data not shown). This chemical modelling rather implies the sorption in the interlayer of several species such as  $\text{Ca}^{2+}$  or  $\text{H}^+$ , but also  $\text{CaCl}^+$  ion pairs. The incorporation of the latter ion pairs at high ionic strength has been demonstrated by Ferrage et al. (2005c) from the resulting modification of XRD reflection intensity distribution and of the layer thickness value. In the present study, no significant change in the reflection relative intensities is observed and the layer thickness value determined for 2W layers is remarkably constant over the whole low-pH range (Fig. 5 - Table 2). However, the XRD modelling approach is not sensitive enough to detect the low amount of sorbed  $\text{CaCl}^+$  species modelled (Fig. 11).

415 The consistency between the XRD modelling and chemical modelling results can be  
416 assessed by calculating the hydration state of the sample from the latter results while  
417 assuming a fixed hydration state for each interlayer cation. At near-neutral pH (pH = 6.41),  
418 interlayers are purely  $\text{Ca}^{2+}$ -saturated and the hydration state of the sample (2W:1W:0W ratio  
419 95:4:1) determined at this pH may be attributed to  $\text{Ca}^{2+}$ -saturated layers. At extremely low pH  
420 (0.14), the 2W:1W:0W ratio is 6:84:10. However, even at this low pH value, a small  
421 proportion of  $\text{Ca}^{2+}$  cations are still sorbed in the smectite interlayer ( $0.004 \text{ mol.kg}^{-1}$  at pH =  
422 0.14), and the 2W present at this low pH value could possibly be related to remaining  $\text{Ca}^{2+}$ -  
423 saturated layers.  $\text{H}_3\text{O}^+$ -saturated layers were thus assumed to be either 1W or 0W in a 89:11  
424 ratio similar to the 84:10 ratio determined from XRD profile modelling. Using these two  
425 hydration states for  $\text{Ca}^{2+}$ - and  $\text{H}_3\text{O}^+$ -saturated layers it is possible to calculate from the  
426 chemical modelling results the proportion of the different layer types as a function of pH (Fig.  
427 12). The excellent agreement found with the data derived from XRD profile modelling  
428 confirms that  $\text{H}_3\text{O}^+$  and  $\text{Ca}^{2+}$  cations do not coexist in a single interlayer, since this  
429 coexistence would induce a significant and strong discrepancy, particularly in the transition  
430 region. This segregation of the different cations in different interlayers corresponds to the  
431 “demixed state” previously described in heteroionic smectites.

432 Based on water adsorption isotherms, Glaeser and Méring (1954) first suspected the  
433 presence of a demixed state in (Na, Ca)-smectites. They demonstrated that  $\text{Na}^+$  and  $\text{Ca}^{2+}$   
434 cations tend to be distributed in different interlayers but the demixing was interpreted as being  
435 incomplete for RH values lower than 75%. These results were confirmed by Levy and Francis  
436 (1975) using XRD, and Mamy and Gaultier (1979) reported a similar behaviour in (K, Ca)-  
437 smectite. More recently, Iwasaki and Watanabe (1988) were able to refine the distribution of  
438  $\text{Na}^+$  and  $\text{Ca}^{2+}$  cations in smectite and smectite-illite MLSs. Assuming that layers with L.Tck.  
439 of  $\sim 15.0 \text{ \AA}$  and  $\sim 12.5 \text{ \AA}$  were Ca- and Na-saturated, respectively, these authors consistently

440 demonstrated that  $\text{Na}^+$  and  $\text{Ca}^{2+}$  cations are distributed in different layers leading to the  
441 occurrence of segregated domains.

442

#### 443 *4.1.2. Mechanism of $\text{H}_3\text{O}^+$ -for- $\text{Ca}^{2+}$ exchange*

444

445 In the observed  $\text{H}_3\text{O}^+$ -for- $\text{Ca}^{2+}$  exchange,  $\text{H}_3\text{O}^+$  cations replace  $\text{Ca}^{2+}$  cations in a layer by layer  
446 process, but there is no information on the influence of a given interlayer content on the  
447 exchange probability in the next interlayer. The presence of almost periodic 2W and 1W  
448 structures systematically suggests a significant segregation in the layer stacking during the  
449 exchange process but there is no information directly available on the evolution of the  
450 segregation during the process. However, the occurrence probabilities of every layer pair can  
451 be calculated from the structure models obtained (Fig. 6 – Drits and Tchoubar, 1990), and it is  
452 especially relevant to follow the segregation of Ca-saturated 2W layers by using the  
453 segregation index  $\text{Sg}(2\text{W})$  defined by Cesari et al. (1965) and more recently by Drits and  
454 Tchoubar (1990):

$$455 \quad \text{Sg}(2\text{W}) = 1 - \frac{1 - P_{2\text{W}-2\text{W}}}{1 - W_{2\text{W}}}, \quad (4)$$

456 where  $W_{2\text{W}} < P_{2\text{W}-2\text{W}} \leq 1$ ,  $W_{2\text{W}}$  being the relative abundance of 2W layers in the sample and  
457  $P_{2\text{W}-2\text{W}}$  the probability for a 2W layer to follow a 2W layer in the layer stacks.  $\text{Sg}(2\text{W})$  ranges  
458 from 1 for a physical mixture and 0 for a random distribution of layers. To account for the n  
459 structures contributing to the diffracted intensity  $W_{2\text{W}}$  is expressed as:

$$460 \quad W_{2\text{W}} = \sum_{i=1}^n [\text{Ab.MLS}^i \times W_{2\text{W}}^i] \quad (5)$$

461 where  $\text{Ab.MLS}^i$  is the relative contribution of the structure  $\text{MLS}^i$ , and  $W_{2\text{W}}^i$  the relative  
462 proportion of 2W layers in this structure. For the global sample  $P_{2\text{W}-2\text{W}}$  is calculated as:

463 
$$P_{2W-2W} = \frac{W_{2W-2W}}{W_{2W}} \quad (6)$$

464 where  $W_{2W-2W}$  is the relative abundance of layer pairs constituted of two  $2W$  layers. Taking  
 465 into account the  $n$  structures contributing to the diffracted intensity, this term is calculated as:

466 
$$W_{2W-2W} = \sum_{i=1}^n [\text{Ab.MLS}^i \times W_{2W-2W}^i] \quad (7)$$

467 In the present study, layer stacking is random in all MLS contributing to the diffracted  
 468 intensity and equation 4 can thus be transformed to:

469 
$$\text{Sg}(2W) = 1 - \frac{1 - \sum_{i=1}^n [\text{Ab.MLS}^i \times (W_{2W}^i)^2] / \sum_{i=1}^n [\text{Ab.MLS}^i \times W_{2W}^i]}{1 - \sum_{i=1}^n [\text{Ab.MLS}^i \times W_{2W}^i]}, \quad (8)$$

470 Note that equation 8 is valid only if all MLS contributing to the diffracted intensity are  
 471 randomly interstratified. As a function of pH, the calculated  $\text{Sg}(2W)$  value ranges from 0.2 to  
 472 0.4 whatever the  $W_{2W}$  value (Fig. 13). This  $\text{Sg}(2W)$  value corresponds to a limited degree of  
 473 segregation, and its stability, within error, throughout the whole pH range, including the  
 474  $\text{H}_3\text{O}^+$ -for- $\text{Ca}^{2+}$  exchange zone, indicates that this cation exchange occurs randomly within the  
 475 crystals with no influence of the interlayer cation present in the adjacent interlayers.

476

477

#### 478 *4.1.3. XRD characterisation of the resulting solid*

479

480 The XRD profile modelling approach used in the present study allowed all of the  
 481 experimental patterns to be reproduced satisfactorily, but it led in a few cases to extremely  
 482 heterogeneous structures, as up to four contributions were sometimes necessary to fit XRD  
 483 profiles. However, in order to reduce the number of adjustable parameters associated with  
 484 these additional contributions, all layers were assumed to have strictly identical properties

485 (layer thickness,  $\sigma_z$ , and H<sub>2</sub>O content) in all contributions for a given sample. In addition, the  
486 size of the CSDs (N) and the preferred orientation parameter ( $\sigma^*$ ) were also identical for the  
487 different MLSs contributing to a given XRD pattern. At each pH value, adjustable parameters  
488 were thus limited to the composition of the different MLSs, and to their relative proportions.  
489 Moreover, when four MLSs were used to fit the experimental XRD patterns (pH = 1.75, 1.48  
490 and 1.28 – Fig. 6), these parameters were found to be consistent from one pH value to the  
491 next. Two of these four contributions correspond to essentially bi- or mono-hydrated smectite  
492 whereas the other two, which account for the heterogeneous layer stacks resulting from the  
493 ongoing exchange process, have approximately constant compositions.

494         The decrease in interlayer thickness fluctuation ( $\sigma_z$  parameter) from 0.35 Å for near  
495 neutral conditions to 0.23 Å (Table 2) for acidic conditions is associated with the hydration  
496 state modification from an essentially bi-hydrated state to an essentially mono-hydrated state.  
497 This correlation is consistent with the observations of Ferrage et al. (2005a) on a  
498 montmorillonite SWy-1 sample saturated with various monovalent and divalent cations.  
499 Indeed, these authors noted that the  $\sigma_z$  parameter is significantly higher (0.25-0.50 Å) when  
500 the sample is dominated by 2W layers than when 0W or 1W layers prevail (0.15-0.25 Å).  
501 They attributed the higher  $\sigma_z$  values determined for 2W layers to their higher layer thickness,  
502 which implies in turn weaker electrostatic interactions between the negatively charged layer  
503 and the interlayer cations. As a consequence, the respective positions of two adjacent 2:1  
504 layers are weakly constrained and the resulting variation of layer thickness from one  
505 interlayer to the adjacent one is enlarged. This phenomenon is likely to occur also for 1W  
506 layers, but the lower layer thickness values and the different location of H<sub>2</sub>O molecules  
507 considerably reduce the screening of electrostatic interactions between the 2:1 layer and the  
508 interlayer cations.



509 In addition, Ferrage et al. (2005a) have observed higher  $\sigma_z$  values at the transition  
510 between two individual hydration states, possibly as a result of the coexistence, within a  
511 single interlayer, of different hydration states resulting in a high degree of fluctuation in the  
512 interlayer thickness. On the contrary, in the present study, the  $\sigma_z$  values steadily decrease with  
513 decreasing pH even over the  $\text{H}_3\text{O}^+$ -for- $\text{Ca}^{2+}$  exchange zone characterised by heterogeneous  
514 structures. Such an even decrease is indicative of the homogeneous hydration state of each  
515 interlayer, that is of the mutual exclusion of  $\text{Ca}^{2+}$  and  $\text{H}_3\text{O}^+$  cations in a single interlayer,  
516 again suggesting a layer-by-layer exchange process leading to a "demixed" state (Glaeser and  
517 Méring, 1954; Levy and Francis, 1975; Mamy and Gaultier, 1979; Iwasaki and Watanabe,  
518 1988). This is also consistent with the constant layer thickness values determined for both 1W  
519 and 2W layers throughout the low-pH range (Table 2).

520 In addition, the number of layers in the CSDS also increases from  $\sim 8.7$  under neutral  
521 conditions to  $\sim 10.0$  under acidic conditions. This steady increase with the transition from a bi-  
522 hydrated state to a mono-hydrated state is consistent with the decreasing N values determined  
523 by Ferrage et al. (2005a, 2005b) for smectite XRD at high RH values when 2W layers prevail,  
524 in agreement with Mystkowski et al. (2000). This evolution can possibly be related to the  
525 breakdown of crystals resulting from the swelling of specific interlayers, which statistically  
526 decreases the crystallite thickness with increasing RH.

527

#### 528 **4.2. Assessment of the presence of $\text{CaOH}^+$ ion pairs in the alkaline pH range**

529

530 The possibility of interlayer  $\text{CaOH}^+$  ion pairs compensating the octahedral charge  
531 under alkaline conditions has been evoked on the basis of cation exchange experiments and  
532 chemical modelling to model the apparent increase of sorbed  $\text{Ca}^{2+}$  at high pH values (Fig. 3 –  
533 Charlet and Tournassat, 2004; Tournassat et al., 2004a, 2004b). However, Ferrage et al.

534 (2005c) has shown that the presence of  $\text{CaCl}^+$  ion pairs similarly evoked for samples  
535 equilibrated with saline solutions (Sposito et al., 1983a 1983b; Tournassat et al., 2004b)  
536 induces significant modification of the experimental XRD patterns. These modifications  
537 affect (i) the intensity ratio between the reflections, as a result of the increase in the electronic  
538 density in the interlayer, (ii) the homogeneity of layer thickness (lower  $\sigma_z$  values), and (iii) the  
539 hydration properties of exchanged smectite, in particular by lowering the relative humidity  
540 value necessary for the bi- to mono-hydrated transition. In addition, the presence of  $\text{CaCl}^+$  ion  
541 pairs may be assessed using NIR-DR spectroscopy from its influence on interlayer  $\text{H}_2\text{O}$   
542 vibration bands. The methodology developed by Ferrage et al. (2005c) to assess the presence  
543 of  $\text{CaCl}^+$  ion pairs in the interlayer of montmorillonite, was applied in the present study to  
544 assess the possible presence of  $\text{CaOH}^+$  ion pairs under high pH conditions.

545

#### 546 *4.2.1. XRD characterisation of the solid*

547

548 Under alkaline conditions, no significant modification of the experimental XRD  
549 patterns is observed as a function of pH and the resulting structure models are similar over the  
550 whole pH range investigated (pH 6.41-12.62). However, it was not possible to keep the layer  
551 thickness of 2W layers constant and a very limited variation was observed (from 15.17 to  
552 15.15 Å), whereas other structural parameters ( $\sigma^*$ ,  $\sigma_z$ , N or water content) were found to be  
553 constant over the whole pH range (Table 3). If  $\text{CaOH}^+$  ion pairs were sorbed in the smectite  
554 interlayers at high pH values, relative reflection intensities in the high-angle region would be  
555 significantly affected, even though the electron density is lower for  $\text{CaOH}^+$  ion pairs ( $28e^-$   
556 /c.u.) than for  $\text{CaCl}^+$  ion pairs ( $36 e^-$ /c.u.). The impact of  $\text{CaOH}^+$  ion pairs on XRD profiles is  
557 illustrated in Figure 14, which shows two patterns calculated for the sample at pH = 12.62.  
558 The first pattern (solid line) is calculated assuming only  $\text{Ca}^{2+}$  as the interlayer cation, whereas

559 the second pattern (grey line) is calculated with  $\text{CaOH}^+$  ion pairs as compensating species, all  
560 other structure parameters being kept constant. The presence of  $\text{CaOH}^+$  ion pairs is clearly  
561 demonstrated by the increase in the 002 and 003 reflection intensity. On the contrary, all  
562 experimental profiles displayed in Figure 9 are similar, and the presence of interlayer  $\text{CaOH}^+$   
563 ion pairs may be dismissed.

564

#### 565 4.2.2. NIR-DR spectroscopy characterisation of the solid

566

567 NIR-DR spectroscopy was used as an independent, complementary technique to  
568 investigate the possibility of  $\text{CaOH}^+$  sorption in montmorillonite interlayer under high-pH  
569 conditions. This technique allows the amount of water and its local interaction with interlayer  
570 species to be studied. In addition, the high sensitivity of infrared spectroscopy for hydroxyls  
571 should allow the detection of partial  $\text{CaOH}^+$ -for- $\text{Ca}^{2+}$  exchange, especially in the hydroxyl  
572 band region. In their study, Ferrage et al. (2005c) showed that when the octahedral charge is  
573 compensated by  $\text{CaCl}^+$  ion pairs instead of  $\text{Ca}^{2+}$  cations, the main modifications to NIR-DR  
574 spectra are: (i) for hydrated samples (40% RH), an increased amount of  $\text{H}_2\text{O}$  induced by the  
575 increased amount of interlayer cationic species and (ii) for out-gassed samples, a shift of  $\text{H}_2\text{O}$   
576 vibration bands induced by the perturbation of the  $\text{H}_2\text{O}$ - $\text{Ca}^{2+}$  interaction by  $\text{Cl}^-$  anions. On the  
577 contrary, the NIR-DR spectra recorded at 0% and ~40% RH for samples obtained at pH 6.41  
578 and 12.62 (Figs. 15, and 16, respectively) are almost identical to each other, whatever the data  
579 collection conditions. In the spectral domain of combinations of  $\text{H}_2\text{O}$  molecules (4550-5500  
580  $\text{cm}^{-1}$ ), the band at 5240-5250  $\text{cm}^{-1}$  can be assigned to  $\text{H}_2\text{O}$  molecules perturbed by interlayer  
581 cations. At 0% RH, this band is still visible, indicating the presence of  $\text{H}_2\text{O}$  molecules despite  
582 the out-gassing conditions (Fig. 15). The residual difference between the spectra recorded for  
583 samples obtained at pH 6.41 and 12.62 (Fig. 15c) reveals a slightly higher amount of  $\text{H}_2\text{O}$

584 molecules in the sample at pH = 6.41. This difference, which probably results from not  
585 strictly identical out-gassing conditions and H<sub>2</sub>O desorption kinetics for the two experiments,  
586 again pleads against the presence of CaOH<sup>+</sup> ion pairs in the smectite interlayer under high-pH  
587 conditions. In the spectral domain of overtones (6500-7500 cm<sup>-1</sup>), similar bands are observed  
588 for the two samples at 6910 and 7090 cm<sup>-1</sup>.

589 As observed under out-gassed conditions, the two spectra recorded at 40% RH for  
590 the same samples are similar (Fig. 16), whereas several modifications between the two sets of  
591 spectra result from the presence of H<sub>2</sub>O molecules. At 40% RH, a shoulder located at  
592 ~5130 cm<sup>-1</sup> is observed for the two samples in the region of combinations (Fig. 16a,b) and the  
593 band observed at 5240 cm<sup>-1</sup> under out-gassed conditions is shifted to 5250 cm<sup>-1</sup>. These two  
594 bands account for the presence of H<sub>2</sub>O molecules weakly adsorbed on interlayer cations and  
595 H-bonded vibrations. Overtones of H<sub>2</sub>O molecules and hydroxyl stretching are also shifted by  
596 the presence of water and are observed at 6830 and 7080 cm<sup>-1</sup> for the two hydrated samples.  
597 As for spectra recorded under out-gassed conditions, the difference between the two spectra  
598 (Fig. 16c) reveals that the amount of H<sub>2</sub>O is again slightly higher in the sample prepared at  
599 pH = 6.41 as compared to the one obtained under high-pH conditions. This difference most  
600 probably results from slightly different experimental conditions rather than from a contrasting  
601 interlayer composition, again pleading against the presence of CaOH<sup>+</sup> ion pairs in the smectite  
602 interlayer under high-pH conditions.

603

#### 604 *4.2.3. Implications on the modelling of the analytical chemistry results for the alkaline pH* 605 *range*

606

607 As discussed above, XRD and NIR-DR spectroscopy results consistently show that  
608 CaOH<sup>+</sup> ion pairs do not enter smectite interlayers at high pH in a calcium cation background.

609 Hence, the analytical chemistry results need to be modelled without the contribution of such  
 610 ion pairs and the modelling results from Tournassat et al. (2004b), accounting for the sorption  
 611 of  $\text{CaOH}^+$  pairs, must be re-examined.

612 Ca-CEC, the apparent CEC in a  $\text{Ca}^{2+}$  cation background (in  $\text{eq.kg}^{-1}$  or  $\text{mol}_c.\text{kg}^{-1}$ ), is  
 613 given by the following equation:

$$614 \quad \text{Ca-CEC} \Leftrightarrow 2 \times \text{Ca}_{\text{sorbed}} \quad (9)$$

615 where  $\text{Ca}_{\text{sorbed}}$  is the amount of Ca sorbed on clay surfaces in  $\text{mol.kg}^{-1}$ . If one assumes that  
 616  $\text{CaOH}^+$  is the only compensating species in smectite interlayers at high pH, the reaction taking  
 617 place during the Ca-CEC measurement experiment is:



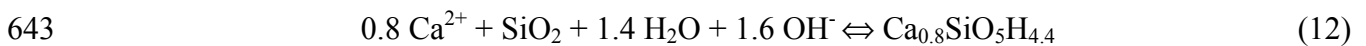
619 where  $\text{X}^-$  represents one mole of the exchanger phase. Then,  $\text{Ca}_{\text{sorbed}} = 2 [\text{Ca}^{2+}]_1/\rho$ , where  
 620  $[\text{Ca}^{2+}]_1$  is the concentration of  $\text{Ca}^{2+}$  released in solution by reaction 10 and determined  
 621 experimentally (Sposito et al., 1981, 1983a). The presence of  $\text{CaOH}^+$  in exchange position  
 622 thus leads to an apparent increase in the Ca-CEC as each Ca in solution is converted to two  
 623 structural charges in the calculation, even though one  $\text{CaOH}^+$  equilibrates only one structural  
 624 charge (Sposito et al., 1983a, 1983b).

625  $\text{CaOH}^+$  exchange also leads to the net consumption of one  $\text{OH}^-$  per sorbed  $\text{CaOH}^+$ ,  
 626 leading to a one-to-one correlation between the change of apparent surface charge  
 627 (disappearance of  $\text{OH}^-$  in  $\text{eq.kg}^{-1}$ ) and that of Ca-CEC (in  $\text{eq.kg}^{-1}$  – reaction 11 – Tournassat et  
 628 al., 2004a, 2004b):



630 Hence, reaction 11 could explain almost perfectly the increase in Ca-CEC as a  
 631 function of pH in the present study and the  $\text{Ca}^{2+}$ -CEC vs. "sorbed"  $\text{OH}^-$  stoichiometry  
 632 observed in the study of Tournassat et al. (2004a, 2004b). This assumption is in contradiction  
 633 with the experimental evidence deduced from XRD and NIR-DR spectroscopy results.

634 As precipitation of a Ca-Si phase can be an alternative explanation for the apparent  
635 increase in Ca sorption and for the decrease in Si concentration occurring under high-pH  
636 conditions, the saturation index of many Calcium-Silicate-Hydrate (CSH – HATCHES, 1998)  
637 were calculated as a function of pH for the solution composition reported in the present study  
638 and in that of Tournassat et al. (2004a). Among the results listed in Table 4, it is possible to  
639 note that both CSH 0.8 and CSH 1.1 (HATCHES, 1998) are oversaturated with respect to the  
640 chemical conditions prevailing in solution. Since CSH 0.8 is closer from its equilibrium ion  
641 activity product than CSH 1.1, the former phase is more likely to precipitate, as described in  
642 the following reaction:



644 The precipitate would remain in the clay slurry during the centrifugation step before  
645 addition of  $\text{NH}_4^+$ . This addition desorbs  $\text{Ca}^{2+}$  from the interlayer and also induces the  
646 dissolution of the CSH 0.8 phase as a result of the pH decrease resulting from the dilution of  
647 the alkaline solution in contact with the clay slurry. In turn, this dissolution leads to the  
648 release of  $\text{Ca}^{2+}$  in solution and to the observed apparent increase in the Ca-CEC. Since  
649 reaction 12 leads to a one-to-one correlation between the change of apparent surface charge  
650 and that of Ca-CEC (disappearance of 1.6 mol<sub>c</sub> of  $\text{OH}^-$  and  $0.8 \times 2 = 1.6$  mol<sub>c</sub> of  $\text{Ca}^{2+}$ ), it may  
651 equally account for the observed  $\text{Ca}^{2+}$ -CEC vs. "sorbed"  $\text{OH}^-$  stoichiometry.

652

## 653 **5. CONCLUSIONS**

654

655 The present study focuses on the modification to the hydration state occurring in Ca-  
656 SWy-2 montmorillonite as a function of pH. Under acidic conditions, a transition from bi-  
657 hydrated to mono-hydrated state was observed, occurring as the result of a  $\text{H}_3\text{O}^+$ -for- $\text{Ca}^{2+}$   
658 exchange in the smectite interlayer. XRD profile modelling was successfully applied to

659 determine the proportion of the different layer types in the reacted samples, even for  
660 extremely heterogeneous hydration states. The proportion of layers obtained was consistent  
661 with that derived from chemical modelling, confirming the latter results and demonstrate the  
662 ability of these two independent methods to accurately characterise chemical/structural  
663 modifications in smectite interlayers. In addition, the exchange between  $\text{Ca}^{2+}$  cations and  
664  $\text{H}_3\text{O}^+$  ions has been shown to occur as a layer-by-layer process, taking place randomly in the  
665 layer stack.

666 Under high-pH conditions, the possible presence of  $\text{CaOH}^+$  ion pairs in the smectite  
667 interlayer is proven to be false from results obtained both by XRD profile modelling and by  
668 NIR-DR spectroscopy. As a consequence, the apparent increase in Ca sorption and the  
669 decrease in Si concentration occurring under high-pH conditions probably result most likely  
670 from the precipitation of a CSH phase, which is thermodynamically favoured.

671

672 *Acknowledgements* – The results presented in the present article were collected during a Ph.D.  
673 thesis granted by ANDRA (French National Agency for Nuclear Waste Disposal). ANDRA is  
674 thanked for its permission to publish this manuscript, and the authors acknowledge its  
675 financial support. The French Geological Survey (BRGM) is acknowledged for its editorial  
676 financial support. EF is grateful to Pr. Boris A. Sakharov for fruitful discussions during XRD  
677 profile modelling. The manuscript was improved by the constructive reviews of two  
678 anonymous reviewers and AE Garrison Sposito, and by the remarks of Emmanuel Jacquot on  
679 an early version of the manuscript.

680

## REFERENCES

- 680  
681
- 682 Appelo, C.A.J. and Postma, D. (2000) *Geochemistry, Groundwater and Pollution*, Rotterdam  
683 press, 536pp.
- 684 Baeyens, B. and Bradbury, M.H. (1997) A mechanistic description of Ni and Zn sorption on  
685 Na-montmorillonite. Part I: Titration and sorption measurements. *J. Contam. Hydrol.*  
686 **27**, 199-222.
- 687 Bérend, I., Cases, J.M., François, M., Uriot, J.P., Michot, L.J., Masion, A. and Thomas, F.  
688 (1995) Mechanism of adsorption and desorption of water vapour by homoionic  
689 montmorillonites: 2. the Li<sup>+</sup>, Na<sup>+</sup>, K<sup>+</sup>, Rb<sup>+</sup> and Cs<sup>+</sup> exchanged forms. *Clays Clay*  
690 *Miner.* **43**, 324-336.
- 691 Bishop, J., Murad, E. and Dyar, M.D. (2002) The influence of octahedral and tetrahedral  
692 cation substitution on the structure of smectites and serpentines as observed through  
693 infrared spectroscopy. *Clay Miner.* **37**, 361-628.
- 694 Bradbury, M.H. and Baeyens, B. (1997) A mechanistic description of Ni and Zn sorption on  
695 Na-montmorillonite. Part II: modeling. *J. Contam. Hydrol.* **27**, 223-248.
- 696 Bradley, W.F., Grim, R.E. and Clark, G.F. (1937) A study of the behavior of montmorillonite  
697 on wetting. *Z. Kristallogr.* **97**, 260-270.
- 698 Burneau, A., Barrès, O., Gallas, J.P. and Lavalley, J.C. (1990) Comparative study of the  
699 surface hydroxyl groups of fumed and precipitated silicas. 2. Characterization by  
700 infrared spectroscopy of the interaction with water. *Langmuir* **6**, 1364-1372.
- 701 Burneau, A. and Carteret, C. (2000) Near infrared and ab initio study of the vibrational modes  
702 of isolated silanol on silica. *Phys. Chem. Chem. Phys.* **2**, 3217-3226.
- 703 Cases, J.M., Bérend, I., François, M., Serekova, Uriot, J.P., Michot, L.J. and Thomas, F.  
704 (1997) Mechanism of adsorption and desorption of water vapour by homoionic



705 montmorillonite: 3. the Mg<sup>2+</sup>, Ca<sup>2+</sup>, Sr<sup>2+</sup> and Ba<sup>2+</sup> exchanged forms. *Clays Clay*  
706 *Miner.* **45**, 8-22.

707 Cesari, M., Morelli, G.L. and Favretto, L. (1965) The determination of the type of stacking in  
708 mixed-layer clay minerals. *Acta Cryst.* **18**, 189-196.

709 Charlet, L. and Tournassat, C. (2005) Fe(II)-Na(I)-Ca(II) cation exchange on montmorillonite  
710 in chloride medium; evidence for preferential clay adsorption of chloride – metal ion  
711 pairs in seawater. *Aquat. Geochem.* (in press).

712 Claret, F., Bauer, A., Schafer, T., Griffault, L. and Lanson, B. (2002) Experimental  
713 Investigation of the interaction of clays with high-pH solutions: a case study from the  
714 Callovo-Oxfordian formation, Meuse-Haute Marne underground laboratory (France).  
715 *Clays Clay Miner.* **50**, 633-646.

716 Cuadros, J. (1997) Interlayer cation effects on the hydration state of smectite. *Am. J. Sci.* **297**,  
717 829-841.

718 Delville, A. (1991) Modeling the clay-water interface. *Langmuir* **7**, 547-555.

719 Drits, V.A. and Sakharov, B.A. (1976) *X-Ray structure analysis of mixed-layer minerals.*  
720 Dokl. Akad. Nauk SSSR, Moscow, 256 pp.

721 Drits, V.A. and Tchoubar, C. (1990) *X-ray diffraction by disordered lamellar structures:*  
722 *Theory and applications to microdivided silicates and carbons.* Springer-Verlag,  
723 Berlin, 371 pp.

724 Drits, V.A., Sakharov, B.A., Lindgreen, H. and Salyn, A. (1997a) Sequential structure  
725 transformation of illite-smectite-vermiculite during diagenesis of Upper Jurassic shales  
726 from the North Sea and Denmark. *Clay Miner.* **32**, 351-371.

727 Drits, V.A., Srodon, J. and Eberl, D.D. (1997b) XRD measurement of mean crystallite  
728 thickness of illite and illite/smectite: reappraisal of the kubler index and the scherrer  
729 equation. *Clays Clay Miner.* **45**, 461-475.

730 Elprince, A.M., Vanselow, A.P. and Sposito, G. (1980) Heterovalent, ternary cation exchange  
731 equilibria:  $\text{NH}_4^+$ - $\text{Ba}^{2+}$ - $\text{La}^{3+}$  exchange on montmorillonite. *Soil Sci. Soc. Am. J.* **44**,  
732 964-969.

733 Ferrage, E., Lanson, B., Sakharov, B.A. and Drits, V.A. (2005a) Investigation of smectite  
734 hydration properties by modeling of X-ray diffraction profiles. Part 1. Montmorillonite  
735 hydration properties. *Amer. Mineral.*, (accepted).

736 Ferrage, E., Lanson, B., Sakharov, B.A., Jacquot, E., Geoffroy, N. and Drits, V.A. (2005b)  
737 Investigation of smectite hydration properties by modeling of X-ray diffraction  
738 profiles. Part 2. Influence of layer charge and charge location, (in preparation).

739 Ferrage, E., Tournassat, C., Rinnert, E., Charlet, L. and Lanson, B. (2005c) Experimental  
740 evidence for calcium-chloride ion pairs in the interlayer of montmorillonite. A XRD  
741 profile modelling approach. *Clays Clay Miner.* (accepted).

742 Fletcher, P. and Sposito, G. (1989) The chemical modeling of clay/electrolyte interactions for  
743 montmorillonite. *Clay Miner.* **24**, 375-391.

744 Gilbert, M. and Laudelout, H. (1965) Exchange properties of hydrogen ions in clays. *Soil Sci.*  
745 **100**, 157.

746 Glaeser, R. and Méring, J. (1954) Isothermes d'hydratation des montmorillonites bi-ioniques  
747 (Ca, Na). *Clay Mineral. Bull.* **2**, 188-193.

748 Guinier, A. (1964) *Théorie et technique de la radiocristallographie*. Dunod, Paris, 740 pp.

749 HATCHES (1998) Harwell/Nirex thermodynamic database for chemical equilibrium studies.

750 Howard, S.A. and Preston, K.D. (1989) Profile fitting of powder diffraction patterns. Pp. 217-  
751 275 in: *Modern Powder Diffraction* (D.L. Bish and J.E. Post, editors). Reviews in  
752 Mineralogy **20**, Mineralogical Society of America, Washington D.C.

753 Iwasaki, T. and Watanabe, T. (1988) Distribution of Ca and Na ions in dioctahedral smectites  
754 and interstratified dioctahedral mica/smectites. *Clays Clay Miner.* **36**, 73-82.

- 755 Kittrick, J.A. (1969a) Interlayer forces in montmorillonite and vermiculite. *Soil Sci. Soc. Am.*  
756 *J.* **33**, 217-222.
- 757 Kittrick, J.A. (1969b) Quantitative evaluation of the strong-force model for expansion and  
758 contraction of vermiculite. *Soil Sci. Soc. Am. J.* **33**, 222-225.
- 759 Laird, D.A. (1996) Model for crystalline swelling of 2:1 phyllosilicates. *Clays Clay Miner.*  
760 **44**, 553-559.
- 761 Laird, D.A. (1999) Layer charge influences on the hydration of expandable 2:1  
762 phyllosilicates. *Clays Clay Miner.* **47**, 630-636.
- 763 Levy, R. and Francis, C.W. (1975) Demixing of sodium and calcium ions in montmorillonite  
764 crystallites. *Clays Clay Miner.* **23**, 475-476.
- 765 Madejova, J., Bujdak, J., Petit, S. and Komadel, P. (2000a) Effects of chemical composition  
766 and temperature of heating on the infrared spectra of Li-saturated dioctahedral  
767 smectites. (I) Mid-infrared region. *Clay Miner.* **35**, 739-751.
- 768 Madejova, J., Bujdak, J., Petit, S. and Komadel, P. (2000b) Effects of chemical composition  
769 and temperature of heating on the infrared spectra of Li-saturated dioctahedral  
770 smectites. (II) Near-infrared region. *Clay Miner.* **35**, 753-761.
- 771 Mamy, J. and Gaultier, J.P. (1979) Etude comparée de l'évolution des montmorillonites  
772 biioniques K-Ca de Camp-Berteaux et du Wyoming sous l'effet des cycles  
773 d'humectation et de dessiccation. *Clay Miner.* **14**, 181-192.
- 774 Méring, J. (1949) L'interférence des rayons-X dans les systèmes à stratification désordonnée.  
775 *Acta Cryst.* **2**, 371-377.
- 776 Mermut, A.R. and Lagaly, G. (2001) Baseline studies of the clay minerals society source  
777 clays: layer-charge determination and characteristics of those minerals containing 2:1  
778 layers. *Clays Clay Miner.* **49**, 393-397.

779 Mooney, R.W., Keenan, A.G. and Wood, L.A. (1952) Adsorption of water vapor by  
780 montmorillonite. II. Effect of exchangeable ions and lattice swelling as measured by  
781 X-ray diffraction. *J. Am. Chem. Soc.* **74**, 1331-1374.

782 Moore, D.M. and Reynolds, R.C., Jr (1997) *X-ray Diffraction and the Identification and*  
783 *Analysis of Clay Minerals*. Oxford University Press, Oxford and New York, 322pp pp.

784 Mystkowski, K., Srodon, J. and Elsass, F. (2000) Mean thickness and thickness distribution of  
785 smectite crystallites. *Clay Miner.* **35**, 545-557.

786 Nagelschmidt, G. (1936) The structure of montmorillonite. *Z. Kristallogr.* **93**, 481-487.

787 Norrish, K. (1954) The swelling of montmorillonite. *Disc. Farad. Soc.* **18**, 120-134.

788 Parkhurst, D.L. and Appelo, C.A.J. (1999) Phreeqc2 user's manual and program U.S.  
789 Geological Survey.

790 Plançon, A. (2002) New modeling of X-ray diffraction by disordered lamellar structures, such  
791 as phyllosilicates. *Amer. Mineral.* **87**, 1672-1677.

792 Sakharov, B.A. and Drits, V.A. (1973) Mixed-layer kaolinite-montmorillonite: a comparison  
793 observed and calculated diffraction patterns. *Clays Clay Miner.* **21**, 15-17.

794 Sakharov, B.A., Lindgreen, H., Salyn, A. and Drits, V.A. (1999) Determination of illite-  
795 smectite structures using multispecimen X-Ray diffraction profile fitting. *Clays Clay*  
796 *Miner.* **47**, 555-566.

797 Shainberg, I., Oster, J.D. and Wood, J.D. (1980) Sodium/calcium exchange in  
798 montmorillonite and Illite suspension. *Soil Sci. Soc. Am. J.* **44**, 960-964.

799 Shu-Yuan, C. and Sposito, G. (1981) The thermodynamics of ternary cation exchange  
800 systems and the subregular model. *Soil Sci. Soc. Am. J.* **45**, 1084-1089.

801 Sposito, G. (1977) The Gapon and Vanselow selectivity coefficients. *Soil Sci. Soc. Am. J.* **41**,  
802 1205-1206.

803 Sposito, G. (1981) *The thermodynamics of soil solution*. Oxford University Press, New  
804 Yorkpp.

805 Sposito, G. (1984) *Surface chemistry of soils*. Oxford University press, New York, 223 pp.

806 Sposito, G., Holtzclaw, K.M., Johnston, C.T. and Le Vesque, C.S. (1981) Thermodynamics of  
807 sodium-copper exchange on Wyoming bentonite at 298 K. *Soil Sci. Soc. Am. J.* **45**,  
808 1079-1084.

809 Sposito, G., Holtzclaw, K.M., Charlet, L., Jouany, C. and Page, A.L. (1983a) Sodium-calcium  
810 and sodium-magnesium exchange on Wyoming bentonite in perchlorate and chloride  
811 background ionic media. *Soil Sci. Soc. Am. J.* **47**, 51-56.

812 Sposito, G., Holtzclaw, K.M., Jouany, C. and Charlet, L. (1983b) Cation selectivity in  
813 sodium-calcium, sodium-magnesium, and calcium-magnesium exchange on Wyoming  
814 bentonite at 298 K. *Soil Sci. Soc. Am. J.* **47**, 917-921.

815 Sposito, G., Skipper, N.T., Sutton, R., Park, S. and Soper, A.K. (1999) Surface geochemistry  
816 of the clay minerals. *Proceedings of the National Academy of Sciences of the United*  
817 *States of America*, **96**, 3358-3364.

818 Stucki, J.W., Golden, D.C. and Roth, C.B. (1984) Effects of reduction and reoxidation of  
819 structural iron on the surface charge dissolution of dioctahedral smectites. *Clays Clay*  
820 *Miner* **32**, 350-356.

821 Tournassat, C., Neaman, A., Villieras, F., Bosbach, D. and Charlet, L. (2003)  
822 Nanomorphology of montmorillonite particles: Estimation of the clay edge sorption  
823 site density by low-pressure gas adsorption and AFM observations. *Amer. Mineral.* **88**,  
824 1989-1995.

825 Tournassat, C., Greneche, J.M., Tisserand, D. and Charlet, L. (2004a) The titration of clay  
826 minerals. Part I. Discontinuous backtitration technique combined to CEC  
827 measurements. *J. Colloid Interf. Sci.* **273**, 224-233.

- 828 Tournassat, C., Ferrage, E., Poinsignon, C. and Charlet, L. (2004b) The titration of clay  
829 minerals. Part II. Structural-based model and implications for clay reactivity. *J.*  
830 *Colloid Interf. Sci.* **273**, 234-246.
- 831 Van Olphen, H. (1965) Thermodynamics of interlayer adsorption of water in clays. *J. Colloid*  
832 *Interf. Sci.* **20**, 822-837.
- 833 Vanselow, A.P. (1932a) Equilibria of the base-exchange reaction of bentonites, permutites,  
834 Soil colloids and zeolites. *Soil Sci.* **33**, 95-113.
- 835 Vantelon, D., Pelletier, M., Michot, L.J., Barres, O. and Thomas, F. (2001) Fe, Mg and Al  
836 distribution in, the octahedral sheet of montmorillonites. An infrared study in the OH-  
837 bending region. *Clay Miner.* **36**, 369-379.
- 838 Walker, G.F. (1956) The mechanism of dehydration of Mg-vermiculite. *Clays Clay Miner.* **4**,  
839 101-115.
- 840

## FIGURE CAPTIONS

840  
841  
842  
843  
844  
845  
846  
847  
848  
849  
850  
851  
852  
853  
854  
855  
856  
857  
858  
859  
860  
861  
862

**Fig. 1.** Schematic description of the strategy used to fit experimental XRD patterns (see text for details). Intensities in the high-angle region ( $10\text{-}50^\circ 2\theta$ ) are enlarged ( $\times 10$ ) compared to the low-angle region ( $4\text{-}10^\circ 2\theta$ ). Qz indicates the presence of quartz. **a)** Experimental pattern of Ca-SWy-2 sample equilibrated in deionised water (pH = 6.41) is shown as crosses whereas the XRD pattern calculated for a periodic bi-hydrated structure (100% bi-hydrated layers – 2W) is shown as a solid line. **b)** Addition of a mixed layer structure (solid grey line) with a 60:30:10 ratio between 2W:1W:0W layers. **c)** Optimum fit to the experimental pattern corresponding to the combination of the above two structures in a 87:13 ratio (solid line). **d)** Schematic representation of the structure model used to fit the experimental XRD pattern. Relative proportions, expressed in wt%, of the two elementary contributions are plotted on the y-axis whereas their compositions (relative proportions of the different layer types) are plotted on the x-axis. Light grey, dark grey and solid bars represent 0W, 1W, and 2W layers, respectively.

**Fig. 2.** Calcium concentration in solution equilibrated with clay suspension as a function of pH (**a**). Aluminium, iron and magnesium concentrations in solution equilibrated with clay suspension as a function of pH (**b**).

**Fig. 3.** Apparent amount of calcium sorbed on smectite and Si concentration in solution as a function of pH.

**Fig. 4.** Evolution of the 001 reflection of equilibrated Ca-SWy-2 as a function of pH. **a)** Under acidic conditions. **b)** Under alkaline conditions.

863 **Fig. 5.** Comparison between experimental and calculated XRD patterns as a function of pH  
864 under acidic conditions. Experimental XRD patterns are shown as crosses whereas  
865 the optimum fits are shown as solid lines.

866 **Fig. 6.** Structure models obtained from XRD profile modelling for samples prepared under  
867 acidic conditions. Symbols and notations as for Figure 1d.

868 **Fig. 7.** Respective contributions of the various mixed-layer structures (MLSs) to the  
869 calculated profiles. Intensities in the high angle region ( $10-50^\circ 2\theta$ ) are enlarged ( $\times 10$ )  
870 as compared to the lower angle region ( $2-10^\circ 2\theta$ ). The different MLSs are shown as  
871 bold, light grey, dark grey and thin solid lines, experimental data are shown as  
872 crosses. **a)** pH = 1.93. **b)** pH = 1.75. **c)** pH = 1.41. **d)** pH = 1.28. **e)** pH = 0.14.

873 **Fig. 8.** Relative proportion of the different layer types obtained from XRD profile modelling  
874 as a function of pH. Solid squares: 2W layers; dark grey squares: 1W layers; light  
875 grey squares: 0W layers.

876 **Fig. 9.** Comparison between experimental and calculated XRD patterns as a function of pH  
877 under alkaline conditions. Symbols as for Figure 5.

878 **Fig. 10.** Structure models obtained from XRD profiles modelling for samples prepared under  
879 alkaline conditions. Symbols and notations as for Figure 1d.

880 **Fig. 11.** Apparent amount of Ca sorbed on smectite as a function of pH. Experimentally  
881 determined values: open squares. Results of the exchange modelling using the  
882 modelling approach developed by Tournassat et al. (2004a) are shown as bold solid  
883 lines ( $\text{Ca}^{2+}$ ), dashed lines ( $\text{H}^+$ ), and solid lines ( $\text{CaCl}^+$ ).

884 **Fig. 12.** Comparison between the relative abundance of the different layer types obtained  
885 from XRD profile modelling (symbols) and that derived from chemical modelling  
886 (solid lines), as a function of pH. Light grey, dark grey and black colours correspond  
887 to 0W, 1W, and 2W layers, respectively



888 **Fig. 13.** Relative abundance of 2W layers obtained from XRD profile modelling (solid  
889 squares) and segregation index of 2W layers ( $Sg(2W)$  – solid diamonds) as a  
890 function of pH under acidic conditions.

891 **Fig. 14.** Comparison between the experimental pattern of the sample prepared at pH = 12.62  
892 (crosses) with those calculated  $Ca^{2+}$  cations (solid line) or  $CaOH^+$  ion pairs (solid  
893 grey line) as the sole charge compensating species.

894 **Fig. 15.** NIR-DR spectra of out-gassed samples. **a)** Sample prepared under near-neutral  
895 conditions (pH = 6.41). **b)** Sample prepared under alkaline conditions (pH = 12.62).  
896 **c)** Difference between the above two spectra ( $c = b - a$ ).

897 **Fig. 16.** NIR-DR spectra of hydrated samples ( $RH = 40 \pm 5\%$ ). **a)** Sample prepared under  
898 near-neutral conditions (pH = 6.41). **b)** Sample prepared under alkaline conditions  
899 (pH = 12.62). **c)** Difference between the above two spectra ( $c = b - a$ ).

**Table 1.** Cation exchange reaction selectivity coefficients ( $K_{int}$ ) used for chemical composition modelling.

Exchange reactions	$\log K_{int}$
$2 \text{HX} + \text{Ca}^{2+} \Leftrightarrow \text{CaX}_2 + 2 \text{H}^+$	0.4 <sup>§</sup>
$\text{HX} + \text{CaCl}^+ \Leftrightarrow \text{CaClX} + \text{H}^+$	2.5 <sup>§</sup>

<sup>§</sup> from Tournassat et al. (2004a)

**Table 2.** Optimum structure parameters determined from the fitting of XRD profiles recorded for samples prepared under acidic conditions.

pH	LT 2W	LT 1W	LT 0W	N	$\sigma^*$	$\sigma_z$	nH <sub>2</sub> O 2W	nH <sub>2</sub> O 1W
6.41	15.18	12.60	10.00	8.7	6.5	0.35	2×3.2	3.2
5.98	15.18	12.60	10.00	8.7	6.3	0.35	2×3.2	3.2
4.73	15.18	12.60	10.00	8.8	6.3	0.35	2×3.2	3.2
2.88	15.18	12.60	10.00	8.9	6.1	0.31	2×3.2	3.2
2.46	15.18	12.60	10.00	8.9	6.0	0.31	2×3.2	3.2
2.23	15.18	12.60	10.00	8.9	6.0	0.30	2×3.2	3.2
2.08	15.18	12.60	10.00	8.9	5.8	0.30	2×3.2	3.2
1.93	15.18	12.60	10.00	8.9	5.8	0.28	2×3.2	3.2
1.75	15.18	12.60	10.00	8.9	5.8	0.26	2×3.2	3.3
1.41	15.18	12.60	10.00	8.9	5.6	0.23	2×3.2	3.3
1.28	15.18	12.60	10.00	9.8	5.6	0.23	2×3.2	3.3
0.98	15.18	12.60	10.00	10.0	6.1	0.23	2×3.2	3.3
0.14	15.18	12.60	10.00	10.0	6.1	0.23	2×3.2	3.3

Note: Layer thickness (LT) of bi-hydrated, mono-hydrated and dehydrated layers (2W, 1W and 0W layers, respectively) are given in Å. For hydrated layers, the amount of interlayer H<sub>2</sub>O molecules is given per O<sub>20</sub>(OH)<sub>4</sub>. N is the mean number of layers in the coherent scattering domains, while the orientation parameter  $\sigma^*$  and layer thickness variability parameter  $\sigma_z$  are given in ° and in Å, respectively.

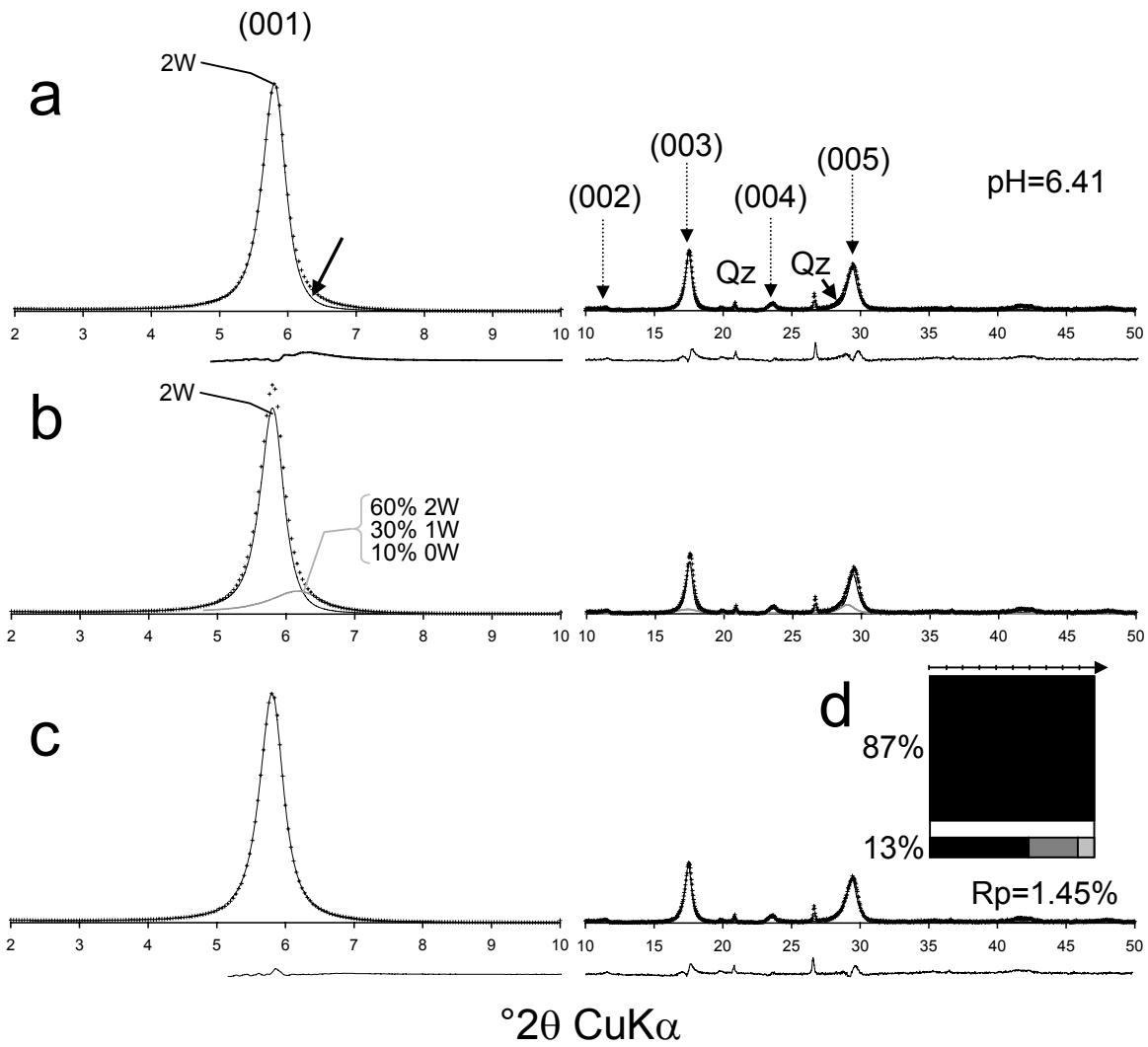
**Table 3.** Optimum structure parameters determined from the fitting of XRD profiles recorded for samples prepared under alkaline conditions.

pH	LT 2W	LT 1W	LT 0W	N	$\sigma^*$	$\sigma_z$	nH <sub>2</sub> O 2W	nH <sub>2</sub> O 1W
6.41	15.18	12.60	10.00	8.7	6.5	0.35	2×3.2	3.2
7.46	15.17	12.60	10.00	9.0	6.5	0.35	2×3.2	3.2
9.59	15.17	12.60	10.00	9.0	6.5	0.35	2×3.2	3.2
11.24	15.16	12.60	10.00	9.1	6.5	0.35	2×3.2	3.2
11.81	15.15	12.60	10.00	9.4	6.0	0.35	2×3.2	3.2
12.31	15.15	12.60	10.00	9.4	5.5	0.35	2×3.2	3.2
12.62	15.15	12.60	10.00	9.3	5.0	0.35	2×3.2	3.2

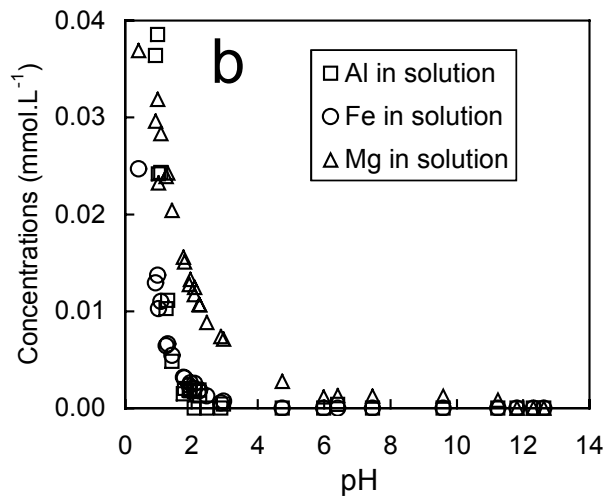
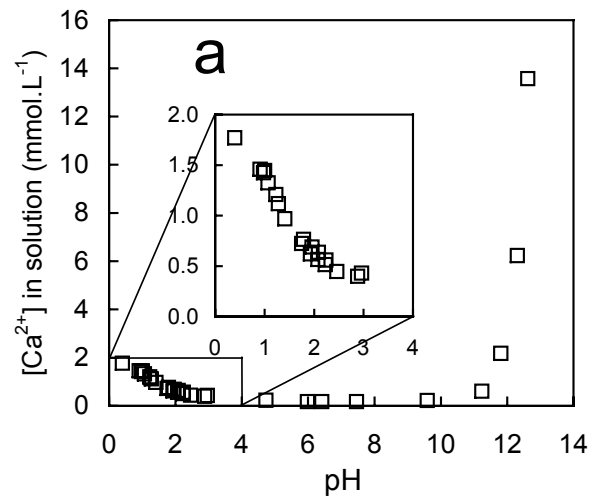
Note: Layer thickness (LT) of bi-hydrated, mono-hydrated and dehydrated layers (2W, 1W and 0W layers, respectively) are given in Å. For hydrated layers, the amount of interlayer H<sub>2</sub>O molecules is indicated per O<sub>20</sub>(OH)<sub>4</sub>. N is the mean number of layers in the coherent scattering domains, while the orientation parameter  $\sigma^*$  and layer thickness variability parameter  $\sigma_z$  are given in ° and in Å, respectively.

**Table 4.** Saturation index (SI) calculated for two CSH phases as a function of pH. Ca and Si concentration conditions measured in the present study and in that of Tournassat et al. (2004a) have been used.

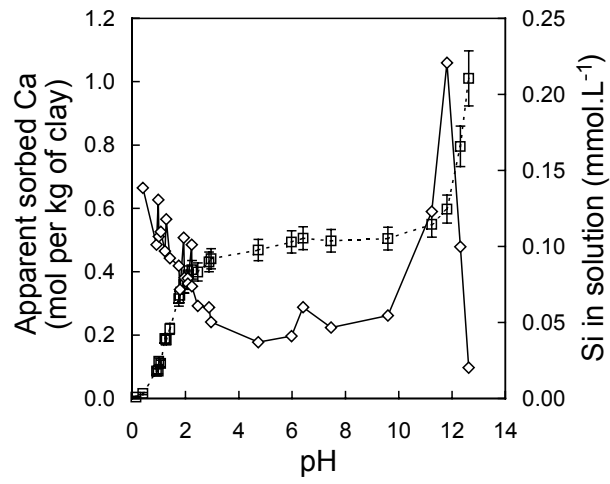
pH	[Ca] (mmol.L <sup>-1</sup> )	[Si] (mmol.L <sup>-1</sup> )	log SI CSH 0.8	log SI CSH 1.1
<i>This study</i>				
11.81	2.18	0.221	0.0	0.6
12.31	6.23	0.100	0.1	1.1
12.62	13.57	0.020	-0.4	0.9
<i>Tournassat et al. (2004a) study</i>				
11.38	5.61	0.68	0.5	1.0
11.93	4.41	0.25	0.3	1.0
10.77	50.8	0.22	0.2	0.5
11.16	50.1	0.14	0.2	0.7



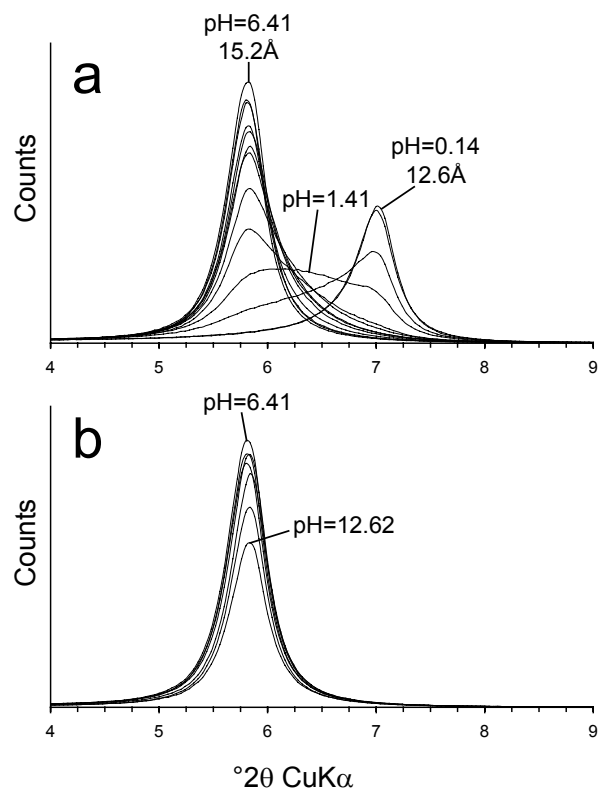
Please print in 2 column format



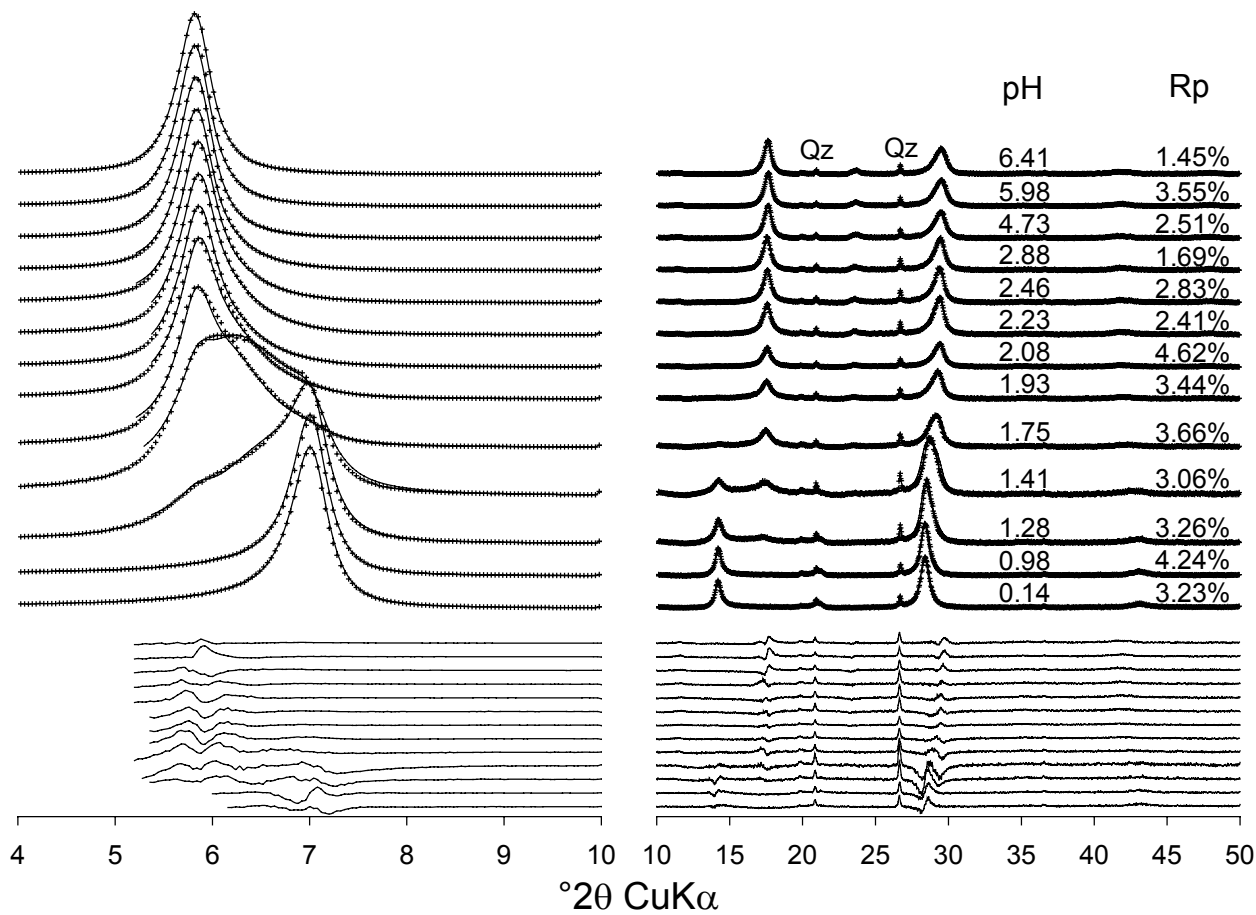
Ms#W2963 Ferrage et al. Fig. 02



Ms#W2963 Ferrage et al. Fig. 03



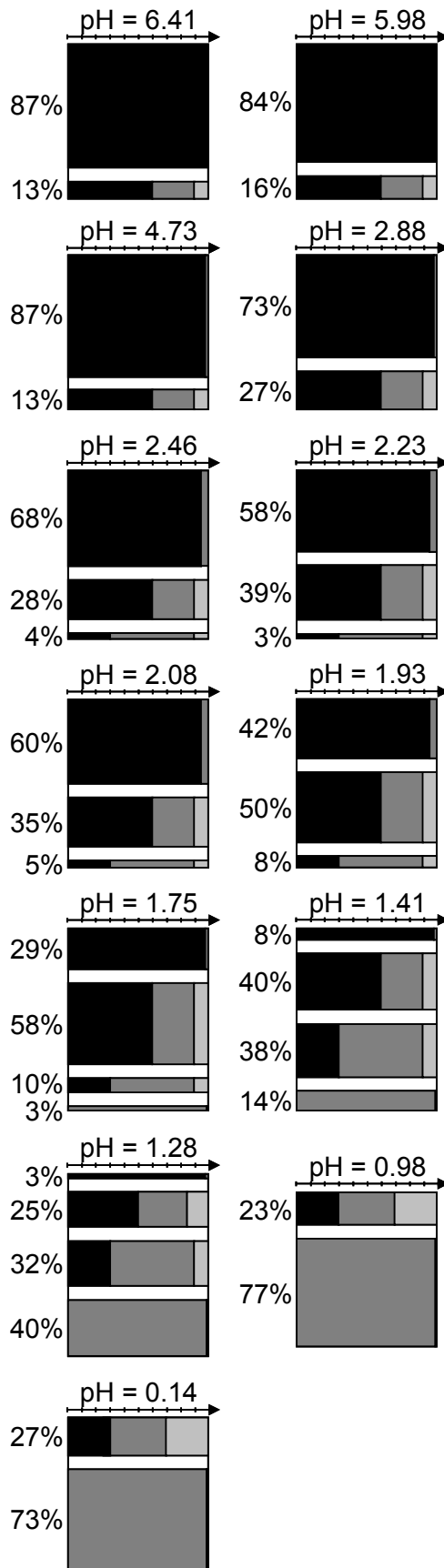
Ms#W2963 Ferrage et al. Fig. 04



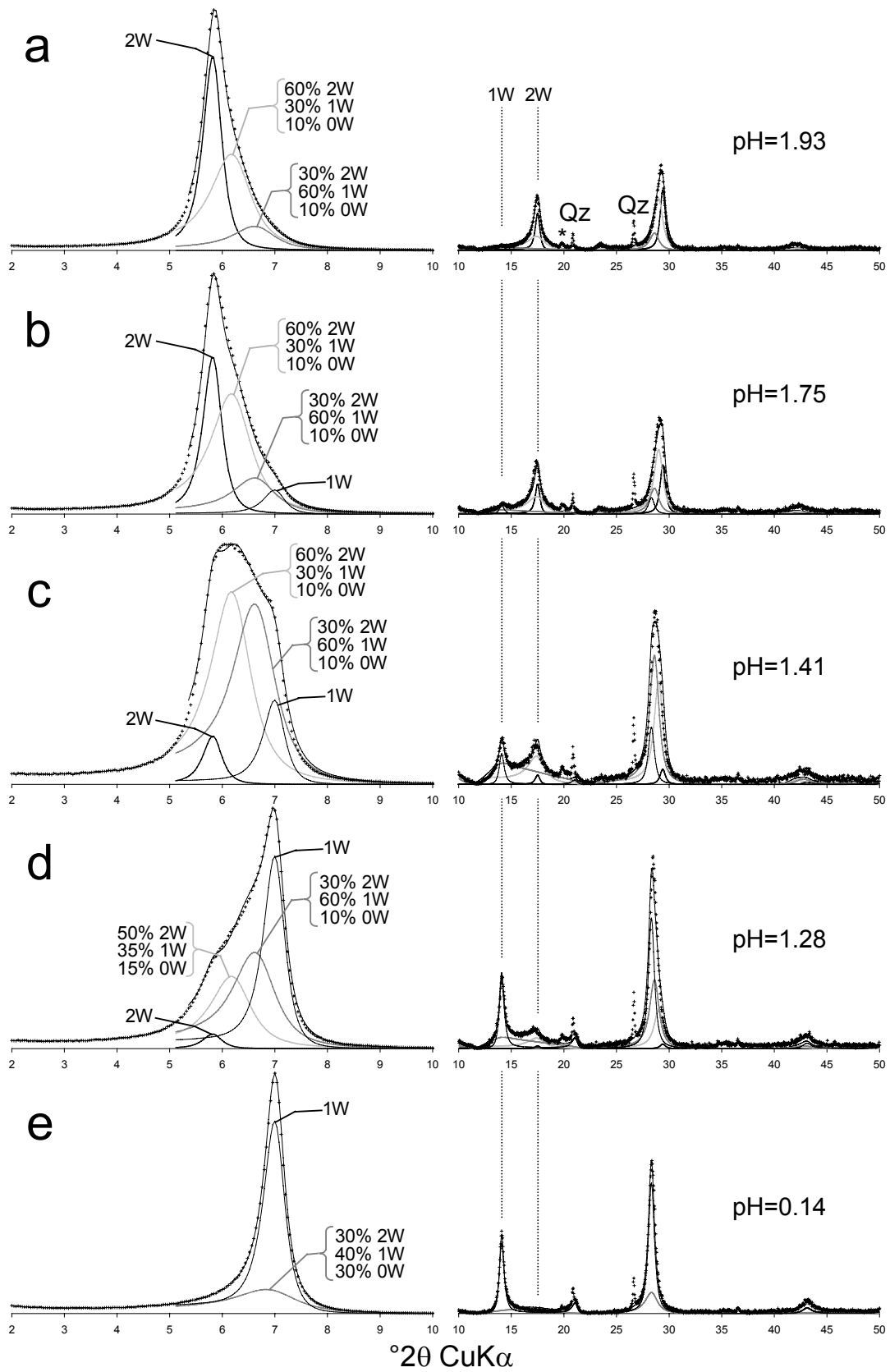
Please print in 2 column format

Ms#W2963 Ferrage et al. Fig. 05

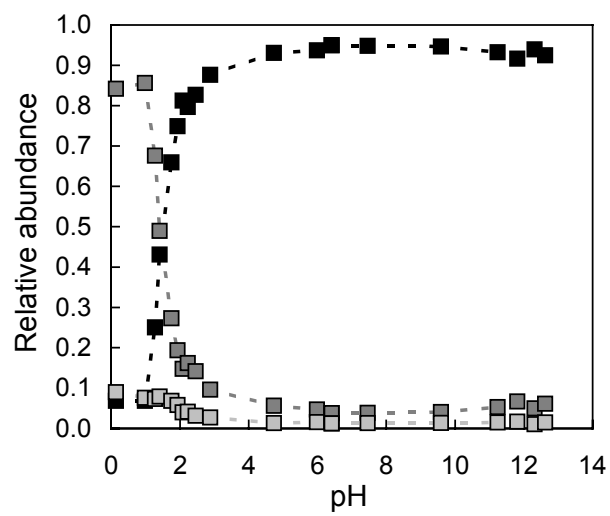




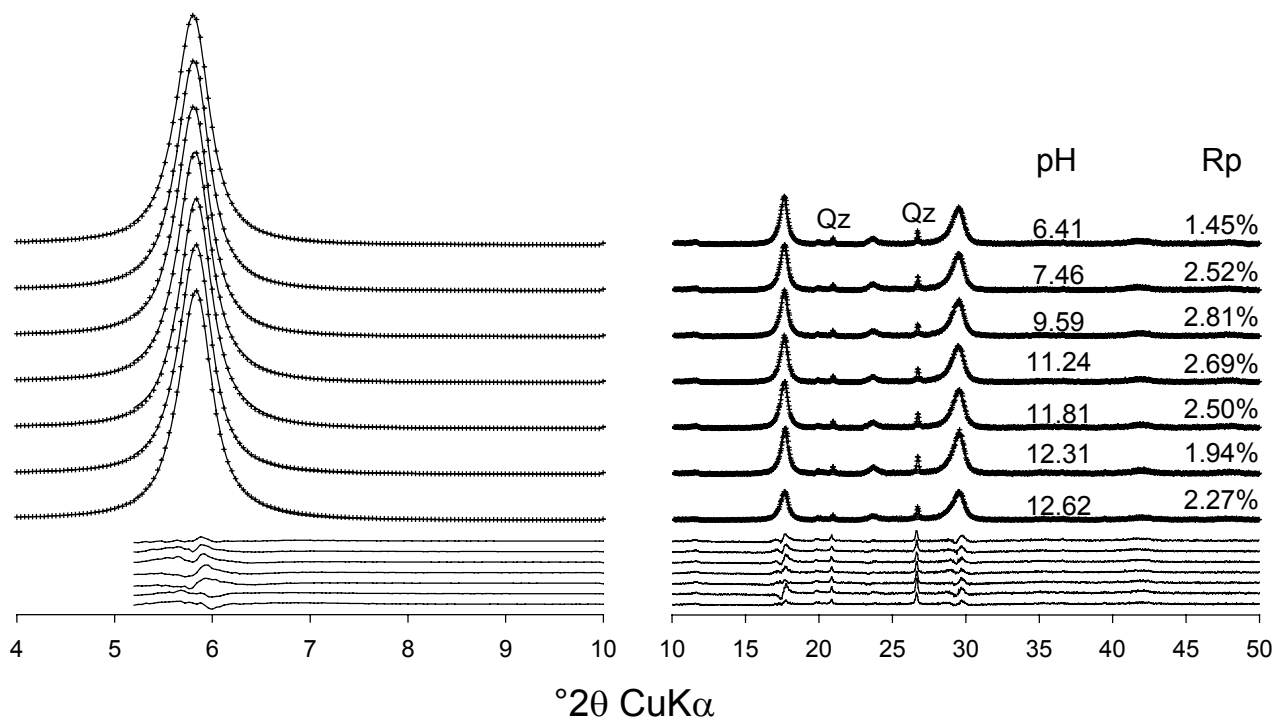
Ms#W2963 Ferrage et al. Fig. 06



Please print in 2 column format

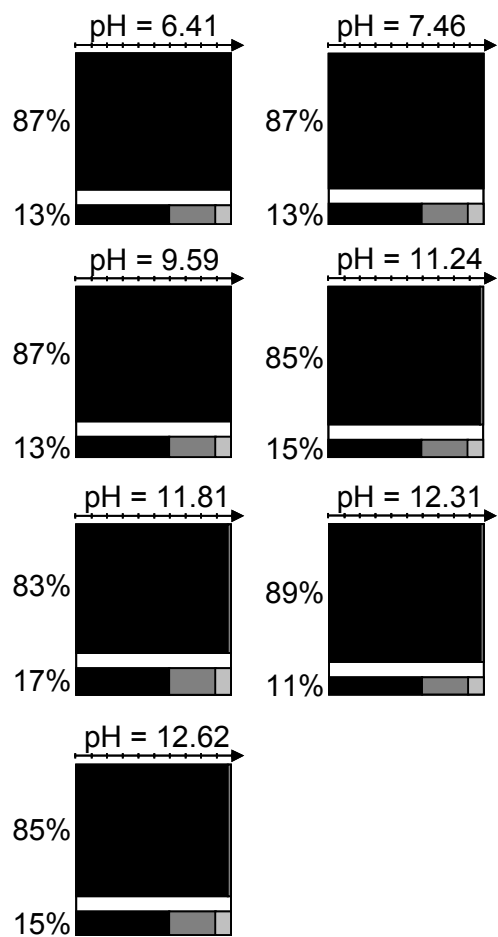


Ms#W2963 Ferrage et al. Fig. 08

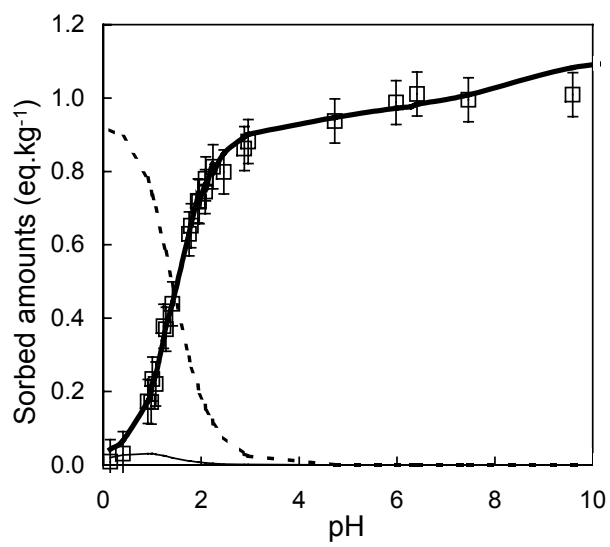


Please print in 2 column format

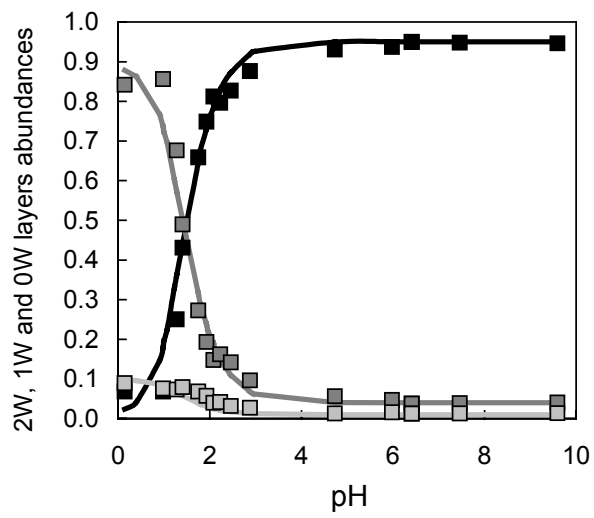
Ms#W2963 Ferrage et al. Fig. 09



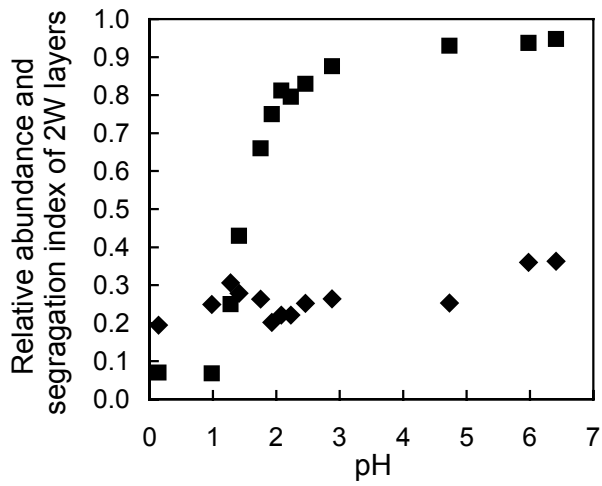
Ms#W2963 Ferrage et al. Fig. 10



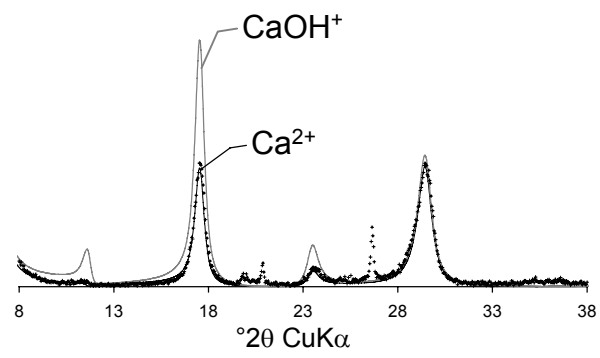
Ms#W2963 Ferrage et al. Fig. 11



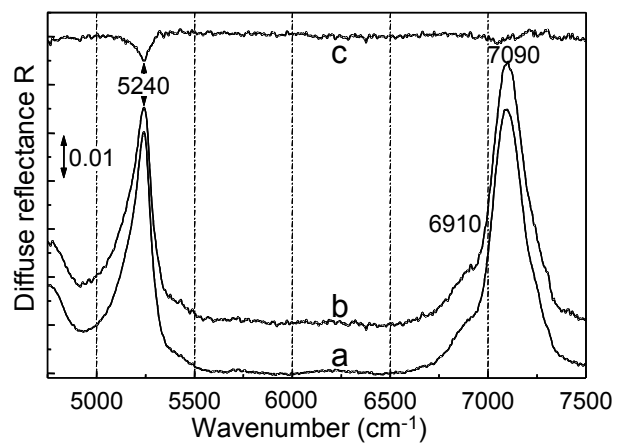
Ms#W2963 Ferrage et al. Fig. 12



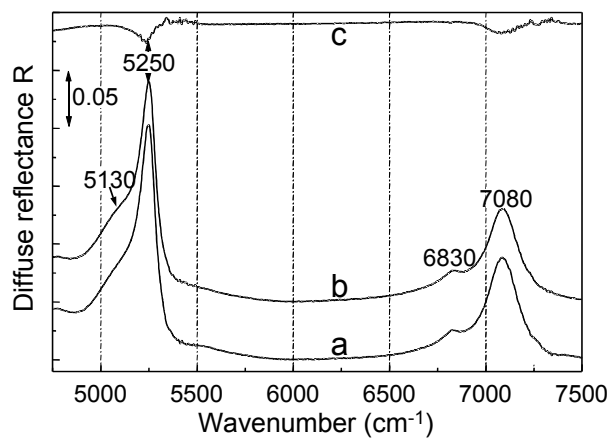




Ms#W2963 Ferrage et al. Fig. 14



Ms#W2963 Ferrage et al. Fig. 15



Ms#W2963 Ferrage et al. Fig. 16